AN INVESTIGATION OF MEVVA IMPLANTED GERMANIUM BY SCANNING PROBE MICROSCOPY, ION BEAM ANALYSIS AND X-RAY DIFFRACTION

A Thesis presented for the partial fulfilment
of the requirements for the degree of
Master of Philosophy

at

The Chinese University of Hong Kong

by

LEE, Chun-Sing (BEng)

Department of Electronics Engineering
The Chinese University of Hong Kong

December, 1998

香港中文大學
大學
圖書館系統
★
21 FEB 2000
UNIVERSITY
LIBRARY SYSTEM
THE CHINESE UNIVERSITY OF HONG KONG

ACKNOWLEDGEMENTS

I would like to express my sincere gratitude to my supervisor, Professor Ian Horward Wilson, for his patient guidance and valuable advice. During the last two years, although Professor Wilson was so busy being a professor and the division head of the graduate division, he has been spending his valuable time to have a weekly meeting with us to give us suggestions. By the same time, Professor has also given me enough space and freedom to work on my own pace. I am indebted to him for his generous patience regarding to my delay on the submission of this thesis.

Special thanks are entitled to my enlightening teachers, Dr Jian-Bin Xu for his helpful guidance on scanning probe microscopy and Dr Sai-Peng Wong for his valuable advice.

I would like to thank Dr Wing-Yiu Cheung for his advice, valuable discussions and assistance in sample preparations and measurements. Thanks to Dr. Yun-Jia Chen for his precious discussions and teaching on the atomic force microscopy. Thanks are extended to Dr E. Z. Luo and Dr Sundaravel for their help in maintaining the RBS system and performing non-Rutherfold scattering experiments and PIXE. Thanks also to Mr W. K. Chan and Dr Ning Ke for their lab assistance.

Thanks to my lab mates, Mr Kwong-Yu Lai, Mr Man-Fat Chiah, Miss L. C. Ho, Mr Venugopal, Mr Di-Hu Chen, Mr Guang-Da Hu, Mr Song Lin and Mr Chi-Pui Li.

Last but not least, I wish to thank my parents for their spiritual and financial support throughout the course of my whole education.

ABSTRACT

In this research, three projects have been carried out to study the ion-bombardment-induced damage and topographic development, ion beam synthesised semiconductor alloy, and tip artifacts in atomic force microscope imaging:

(1) Ion beam implanted germanium by various ion species has been studied by atomic force microscopy (AFM), and Rutherford backscattering spectrometry (RBS). A metal vapour vacuum arc (MEVVA) ion source implanter has been used to implant Co, C, and Ge at an extraction voltage of 60kV into chemomechanically polished Ge(100) n-type wafers with doses ranging from 6×10^{14} to 6×10^{17} ions cm^{-2}, with mean current density being 15 $\mu A\ cm^{-2}$. Cellular nanostructures were observed on both Co-implanted and self-implanted samples, but not in C-implanted ones. This is attributed to the much smaller mass and size of C-ions. Various mechanisms for crater formation are discussed, with special attention paying to whether the larger craters can be created by the coalescence of smaller craters in medium dose implantation (10^{15} – 10^{16} ion cm^{-2}), and also the importance of the thermal spike effect in crater formation. Ion channeling spectra for C-implanted samples show a smaller depth of damaged layer than the Co-implanted and self-implanted samples in higher dose implantation (6×10^{16} – 6×10^{17} ion cm^{-2}). It is contradictory to the theoretical prediction and possible explanations are suggested. A surface yield deficit exists in the random spectra of Co-implanted, and self-implanted samples.

(2) Germanide formation and structural evolution in Co-implanted germanium have been studied by θ-2θ x-ray-diffraction (XRD), Rutherford backscattering spectrometry (RBS) and atomic force microscopy (AFM). A metal vapour vacuum arc (MEVVA) ion source implanter operated at 60 kV was used to

implant Co into Ge(100) wafers with doses ranging from 6×10^{14} to 6×10^{18} ions cm^{-2}, and mean current density being either 15 or 210 $\mu A\ cm^{-2}$. The sequence of phase formations was obtained by XRD. Co_3Ge_2, Co_5Ge_7 and $CoGe_2$ were synthesised in the as-implanted samples. Dramatic cellular and columnar nanostructures were observed by AFM in the low and high mean current density samples respectively. Information on the roughness was obtained. The degree of crystallinity and the depth of the damaged layer were determined by RBS and ion channeling. The phase formation and evolution are discussed with respect to beam heating effect and the heat of formation.

(3) Contact-mode AFM was used to observe the nanostructures created on Ge surfaces by Co-ion implantation in the previous experiments. It was demonstrated that the appearance of a granular morphology obtained by contact mode is due to severe image distortions when the tip size is larger than the mean crater diameter. For images observed by tapping mode AFM, low to medium dose samples (up to 1×10^{16} ions cm^{-2}) may upon to minor image distortions. These tip artifacts can be deconvoluted by inverting the image and the lateral extension of the hole can be reproduced with reasonable accuracy.

摘要

本論文是由三個獨立的研究報告所構成。研究對象包括：離子注入引起的半導體表面損壞及形狀發展；離子注入複合而成的半導體合金；以及原子力顯微鏡探針造成的圖像失真等。

(1)利用金屬蒸氣真空弧注入器，對(100) n 型的鍺(Ge)片進行了鈷(Co)、炭(C)、鍺三種離子注入。引出壓為 6 萬伏，劑量由 6×10^{14} 至 6×10^{17} 離子/平方厘米，電流密度為 15 微安培/平方厘米。並進行了原子力顯微鏡掃描及盧瑟福背向散射研究。結果顯示由於炭粒子的質量較小，只有鈷及鍺作注入的樣品表面形成了環狀的微型結構。報告中討論了不同的環孔形成機制，尤其對小環孔聯成大環孔的可能性，「熱尖鋒」對環孔形成的重要性等，作了較深入的探討。從盧瑟福背向散射譜可看到以炭作高劑量注入的樣品，其損壞層比其他物料注入的樣品為薄。報告對此亦作出不同的解釋。

(2)利用金屬蒸氣真空弧注入器，對(100)的鍺片進行了鈷離子注入。引出壓為 6 萬伏，劑量由 6×10^{14} 至 6×10^{18} 離子/平方厘米，電流密度為 15 或 210 微安培/平方厘米。並進行了 X 射線衍射實驗、原子力顯微鏡掃描及盧瑟福背向散射研究。從樣品中發現了 Co_3Ge_2、Co_5Ge_7 和 $CoGe_2$。環狀和柱狀的微型結構分別於低和高電流密度的樣品表面形成。樣品表面的粗糙度亦被測量。通過盧瑟福背向無規散射及離子信道散射實驗，亦測量了樣品的結晶度和損壞層厚度。報告亦討論了離子束加熱效應及生成熱數值大小對相位形成和發展的影響。

(3)利用接觸式原子力顯微鏡，對鈷離子注入的樣品作表面掃描。結果顯示粒狀結構是由於探針半徑比環孔大，而引致的圖像失真。低至中

劑量(上限為 1×10^{16} 離子/平方厘米)的樣品圖像可能受輕微的失真影響。環孔的大約寬度可從圖像的倒置影像而獲得。

TABLE OF CONTENTS

ACKNOWLEDGEMENTS 2

ABSTRACT 3

TABLE OF CONTENTS 7

LIST OF FIGURES 10

LIST OF TABLES 13

CHAPTER 1 INTRODUCTION 14

1.1. Ion implantation 14

1.2. Scope of the thesis 15

CHAPTER 2 BACKGROUND THEORY 17

2.1. Ion stopping 17

2.2. The energy-loss process 17

2.3. Kinematics of binary elastic collision 20

2.4. Nuclear and electronic stopping 21

2.5. Radiation Damage 22

2.6. Spikes 24

2.7. Topography of ion bombarded surface 26

CHAPTER 3 EQUIPMENT REVIEWS 31

3.1. Metal Vapour Vacuum Arc Ion Source Implanter 31

3.2. Atomic Force Microscopy 34

3.3. Rutherford Backscattering Spectrometry 37

3.4. X-ray Diffraction 40

CHAPTER 4 STUDY OF ION BEAM IMPLANTED GERMANIUM BY

ATOMIC FORCE MICROSCOPY AND RUTHERFORD BACKSCATTERING SPECTROMETRY.. 43

4.1. Introduction 43
4.2. Experiments 45
4.3. Results and discussion 47
4.3.1. AFM.. 47
4.3.2. RBS and ion channeling 64
4.4. Conclusions 71

CHAPTER 5 ION BEAM SYNTHESISED COBALT GERMANIDE ALLOY BY METAL VAPOUR VACUUM ARC IMPLANTATION 73

5.1. Introduction 73
5.2. Experiments 74
5.3. Results and discussion 74
5.3.1. XRD 74
5.3.2. AFM.. 78
5.3.3. RBS and ion channeling 82
5.4. Conclusions 87

CHAPTER 6 TIP ARTIFACTS IN ATOMIC FORCE MICROSCOPE IMAGING OF ION BOMBARDED NANOSTRUCTURES ON GERMANIUM SURFACES 89

6.1. Introduction 89
6.2. Experiments 90
6.3. Results and discussion 90
6.4. Conclusions 95

CHAPTER 7 CONCLUSIONS 96

BIBLIOGRAPHY 98

PUBLICATIONS 105

LIST OF FIGURES

FIGURE	CAPTION	PAGE
Fig. 2.1	Schematic of ion stopping and energy-loss process	18
Fig. 2.2	Nuclear and electronic stopping power curve	19
Fig. 2.3	Schematic of binary elastic collision	20
Fig. 2.4	Schematic of the formation of collision cascade by a PKA	24
Fig. 2.5	Schematic of a displacement spike	25
Fig. 2.6	Atom fluxes into and out of an element of solid surface under the action of an ion beam	27
Fig. 2.7	Schematic of the evolution of inclined planes under the action of an ion beam, (a) $\theta < \theta_c$, (b) $\theta > \theta_c$	29
Fig. 3.1	Schematic of the source electrical configuration (After I. G. Brown [58])	32
Fig. 3.2	AFM optical sensing system (After Multimode™ SPM Instruction Manual, Digital Instruments)	35
Fig. 3.3	Interatomic force vs. distance curve (After Introduction to SPM, Park Scientific Instruments)	36
Fig. 3.4	Basic backscattering spectrometry. Experimental geometry (upper figure); Backscattering spectrum (lower figure) (After Handbook of Modern Ion Beam Materials Analysis [76])	38
Fig. 3.5	Diffraction of x-rays by a crystal (After Cullity [77])	41
Fig. 4.1	Tapping mode AFM micrographs of Co-ion implanted Ge at a dose of (a) 1×10^{15} ions cm^{-2}, (b) 6×10^{15} ions cm^{-2}, (c) 1×10^{16} ions cm^{-2}, (d) 6×10^{16} ions cm^{-2}, (e) 1×10^{17} ions cm^{-2}, (f) 6×10^{17} ions cm^{-2}	48
Fig. 4.2	Tapping mode AFM micrographs of C-ion implanted Ge at a dose of (a) 1×10^{15} ions cm^{-2}, (b) 1×10^{16} ions cm^{-2}, (c) 1×10^{17} ions cm^{-2}	50
Fig. 4.3	Tapping mode AFM micrographs of self-ion implanted Ge at a dose of (a) 1×10^{15} ions cm^{-2}, (b) 1×10^{16} ions cm^{-2}, (c) 1×10^{17} ions cm^{-2}	51

Fig. 4.4	(a) Plan view high resolution SEM micrograph of Co-ion implanted Ge(111) at a dose of 5×10^{16} ions cm^{-2}, mean current density of 15 μA cm^{-2} and an extraction voltage of 70kV; (b) Cross-section high-resolution SEM micrograph of Co-ion implanted Ge(111) at a dose of 5×10^{16} ions cm^{-2}, mean current density of 15 μA cm^{-2} and an extraction voltage of 70kV	53 54
Fig. 4.5	Tapping mode AFM micrograph of Ge surface at the boundary between the bombarded and unbombarded areas. Bombarded by Co-ion at a dose of 6×10^{15} ions cm^{-2}, mean current density of 15 μA cm^{-2} and an extraction voltage of 60kV	55
Fig. 4.6	RMS roughness vs dose of different samples. Dotted lines are exponentially fitted curves as a guide to the eyes	56
Fig. 4.7	Schematic illustration showing a) creation of vacancies and interstitials, b) formation of vacancy clusters and interstitial planes, c) collapse of the surface to fill in the vacancies forming a crater and raising of the periphery due to extra planes. o, vacancy; •, interstitials (After Wilson [20])	58
Fig. 4.8	RBS random (R) and ion channeling (C) spectra for, (a) Co-implanted, (b) C-implanted, (c) self-implanted Ge samples at a dose of 1×10^{15}, 1×10^{17} ions cm^{-2}	65
Fig. 4.9	Depth of damaged layer vs dose for the Germanium samples implanted by different ions	67
Fig. 4.10	χ_{min} vs dose for the Germanium samples implanted by different ions	67
Fig. 4.11	Graph of Co-ion concentration profile calculated from Monte Carlo simulation. A dose of 1×10^{17} ions cm^{-2} is taken as an example	69
Fig. 4.12	Simulation of RBS random spectrum using the concentration profile obtained from Monte Carlo simulation	69
Fig. 4.13	Simulation of RBS random spectrum using a concentration	70

profile contained with carbon ions on the surface

Fig. 5.1 XRD spectra of Co implanted Ge at a condition of (a) 6×10^{16} ions cm^{-2}, 210 μAcm^{-2} (b) 6×10^{17} ions cm^{-2}, 210 μAcm^{-2} (c) 6×10^{18} ions cm^{-2}, 210 μAcm^{-2} 76

Fig. 5.2 Binary phase diagram of Co-Ge compound (After M. Hansen *et al.* [47]) 78

Fig. 5.3 Tapping mode AFM micrographs of Co implanted Ge at a condition of (a) 1×10^{16} ions cm^{-2}, 15 μA cm^{-2}, 800nm×800nm (b) 1×10^{17} ions cm^{-2}, 15 μA cm^{-2}, 5μm×5μm, (c) 1×10^{16} ions cm^{-2}, 210 μA cm^{-2}, 1μm×1μm, (d) 1×10^{17} ions cm^{-2}, 210 μA cm^{-2}, 1μm×1μm 79

Fig. 5.4 RMS roughness vs dose for the low and high mean current density samples 81

Fig. 5.5 RBS and ion channeling spectra of Co implanted Ge at a condition of (a) low mean current density, 6×10^{15} ions cm^{-2}, 6×10^{17} ions cm^{-2}, (b) high mean current density, 6×10^{15} ions cm^{-2}, 6×10^{17} ions cm^{-2} 82

Fig. 5.6 Bearing analysis of self-implanted germanium sample, 6×10^{16} ions cm^{-2}, 15 μA cm^{-2}, by AFM software 85

Fig. 5.7 Simulation of RBS random spectrum taking into account of the decrease of Ge density 86

Fig. 5.8 χ_{min} of the low and high mean current density samples and the thickness of the damaged layer of the low mean current density samples 87

Fig. 6.1 (a) Contact mode AFM micrograph of Co-implanted Ge at a dose of 6×10^{16} ions cm^{-2}, 15μA cm^{-2}, (b) Tapping mode AFM micrograph of Co-implanted Ge at a dose of 6×10^{16} ions cm^{-2}, 15μA cm^{-2} 91

Fig. 6.2 Tip details in (a) contact mode AFM, (b) tapping mode AFM 92

Fig. 6.3 Schematic of AFM imaging of large and small crater when compared with tip radius, (a) $R<<r$, (b) $R>r$ or $R\approx r$ 94

Fig. 6.4 An inverted image of Fig. 6.1 (a) 95

LIST OF TABLES

TABLE	CAPTION	PAGE
Table 4.1	Summary of temperature and implantation time of the Co-ion, C-ion and self-ion as-implanted Ge samples	46
Table 4.2	Mean diameter and standard deviation of craters observed in various doses of Co-ion and self-ion implanted Ge	52
Table 4.3	Average number of displaced atoms produced by the projectile using modified Kinchin-Pease displacement damage function and Monte Carlo Simulation	61
Table 4.4	Comparison among the mean diameter of single cascade calculated by modified Kinchin-Pease displacement damage function and Monte Carlo Simulation, and also the mean diameter of the craters observed in AFM micrographs	62
Table 4.5	Mean deposited energy density per atom and the corresponding temperature in degree Celsius	64
Table 5.1	Summary of temperature, implantation time and XRD results of the Co as-implanted Ge samples	75

CHAPTER 1 INTRODUCTION

1.1. Ion Implantation

The properties of semiconductors can be changed by introducing small quantities of dopant atoms. Such changes make semiconductors to be useful for electronic devices. A method is needed to introduce the dopants in a controllable, reproducible way such that it is free from any undesirable side effects. Initially, dopants were diffused into the semiconductors from a surface source such as a doped glass [1]. The dopant concentration at the surface was maintained at solid solubility and therefore, seriously limited the possible dopant distributions that could be obtained. During 1960s, **ion implantation** was developed.

In ion implantation, the dopant atoms are vaporised, accelerated and directed at the semiconductor target. They enter the crystal lattice, collide with target atoms, lose energy and gradually come to rest within the lattice. The destruction on the target lattice is usually recovered by heat treatments such as furnace annealing or rapid thermal annealing, laser annealing, *etc*.

Accompanied with the rapid development in implantation techniques, one area that has aroused much interest is the study of the ion-bombardment-induced damage and topographic development [10-29]. This topic is of fundamental interest as well as practical importance. It finds the technological applications such as the controlled contouring of surfaces, the preparation of surfaces, or even the modification of mechanical and electrical properties of materials.

Ion implantation has also found vast applications in many aspects. In every integrated circuit production line, there are ion implantation systems. Focused ion

beams can be used directly to write dopant patterns without the need of a mask. Low-energy systems have been designed to implant very shallow dopant layers leading to ion beam deposition. High-dose and high-energy implantation has been used to form buried layers of different materials.

1.2. Scope of the thesis

This research started from following Dr Y. J. Chen, a doctoral student of Professor Wilson in 1994-1997, to study ion-bombardment-induced damage and morphological development.

Single-crystal germanium (Ge) was chosen as the target material because it is of high purity, electrically conducting to avoid charge build-up, and has a reasonable high sputtering yield to reduce beam time and ensure self-cleaning of the surface. Cobalt (Co) was used as the bombarding ions in Chen's work. Though he mentioned about implanting with iron (Fe) and germanium (Ge) into germanium, not many results were presented. Therefore different bombarding ions are chosen to see if it would make any difference on morphological development. Carbon (C) is selected because carbon atom is much smaller in size and in mass than cobalt atom. Germanium is also selected so as to eliminate any effect from phase transformation or chemical sputtering. An investigation of the germanium wafers implanted by the three different ions (Co, C, and Ge) with varying doses is presented in Chapter 4.

By using high beam current density, high temperature would be readily achieved and phase transformation is likely to occur. Many studies have been carried out on forming buried metal silicides by implantation [36-38]. Though a picture of Co-implanted Ge by high beam current density was presented in ref. [19,20] by Chen, it was not a complete series and no account for phase transformation has been

included. Therefore, we try to synthesise a germanide layer by direct implantation. For the bombarding ion, we choose the one that can form a germanide with possible technological applications. Cobalt is a promising candidate as one of its phases of cobalt germanide has a very low resistivity and good thermal stability, which is suitable for interconnection in VLSI technology. Moreover, when implanted into Ge, cobalt ions do not form bubbles or blisters, which may complicate our analysis. Therefore cobalt was chosen as the bombarding ion. The results are presented in Chapter 5.

Chapter 6 presents a study on the tip artifacts in atomic force microscopy (AFM). Contact mode AFM was used to observe the nanostructures created on Ge surfaces by Co-ion implantation in the previous experiments. It was demonstrated that the appearance of a granular morphology is due to severe image distortions when the tip size is larger than the mean crater diameter. A simple way to find out the lateral extension is suggested.

Brief introductions on the background theory and equipment reviews are given in Chapter 2 and Chapter 3, respectively. A conclusion is given in Chapter 7.

CHAPTER 2 BACKGROUND THEORY

This chapter is a brief review of the theory in ion-solid interaction. More detailed discussions can be found in the book written by Nastasi, Mayer and Hirvonen [4].

2.1. Ion Stopping

As shown in Fig. 2.1, when an ion (projectile) with incident energy E_0 bombards into a solid (target) surface, it undergoes a series of collisions with the target atoms, loses energy and gradually comes to rest in a certain depth inside the target. In ion implantation, it is not the total distance R travelled by the ion that is of interest but the projection of R normal to the surface (projected range R_p). The distance travelled between collisions and the amount of energy lost are random processes. Hence all ions of a given type and incident energy do not have same projected range. Instead there is a broad distribution in the depths to which each ion can penetrate. The distribution in ranges is referred to as range straggling (ΔR_p).

2.2. The energy-loss process

The energy loss of an energetic ion passing through a solid is due to the followings:

(a) Inelastic collisions with bound electrons of the target

(b) Elastic collisions with bound electrons of the target

(c) Inelastic collisions with nuclei: these lead to bremsstrahlung, nuclear excitation or nuclear reactions

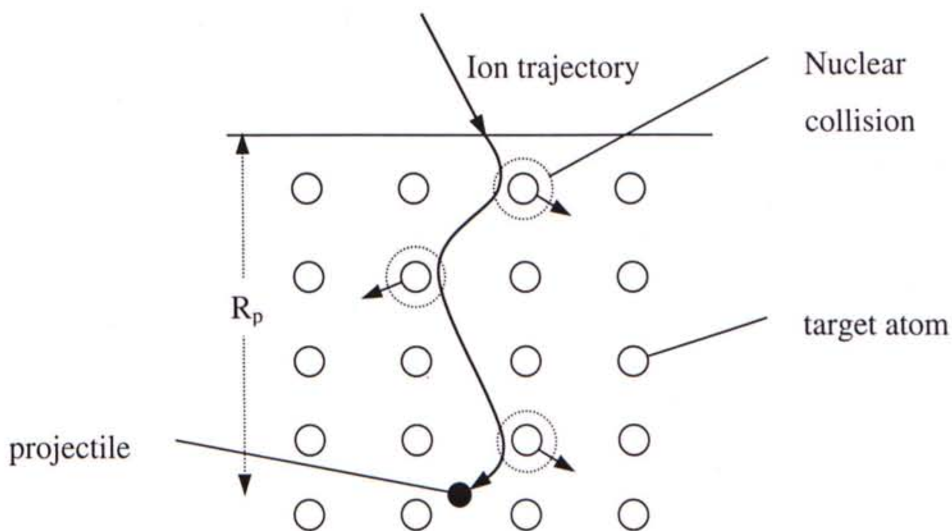

Fig. 2.1 Schematic of ion stopping and energy-loss process
(After Feldman [5])

(d) Elastic collisions with nuclei, whereby part of the kinetic energy is transferred to the target particles

(e) Cerenkov radiation, produced by particles passing through the medium faster than the phase velocity of light

Usually effects of (b), (c) and (e) are much smaller than that of (a) and (d). Therefore, for simplicity, the rate of energy loss is usually expressed as

$$\frac{dE}{dx} = \left.\frac{dE}{dx}\right|_n + \left.\frac{dE}{dx}\right|_e \tag{2.1}$$

where the subscripts n and e denote nuclear elastic collisions and electron inelastic collisions respectively. Nuclear collisions can involve large discrete energy losses and significant angular deflection of the trajectory of the projectile (Fig. 2.1). This process is responsible for the production of lattice disorder by the displacement of the target atoms from their positions in the lattice. Electronic collisions involve much

smaller energy losses per collision, negligible deflection of the ion trajectory, and negligible lattice disorder.

The relative importance of the two energy-loss mechanisms depends very much on the energy E and atomic number Z_1 of the projectile as shown in Fig. 2.2. Nuclear stopping predominates for low E and high Z_1, whereas electronic stopping takes over for high E and low Z_1. E_1 is the energy where the nuclear stopping power is a maximum, E_2 is the energy where the electronic and nuclear stopping power are equal, and E_3 is the energy where the electronic stopping power is maximum. Typical values for Co implanted into Ge are: $E_1 \sim 100$ keV, $E_2 \sim 500$ keV, $E_3 \sim 100$ MeV.

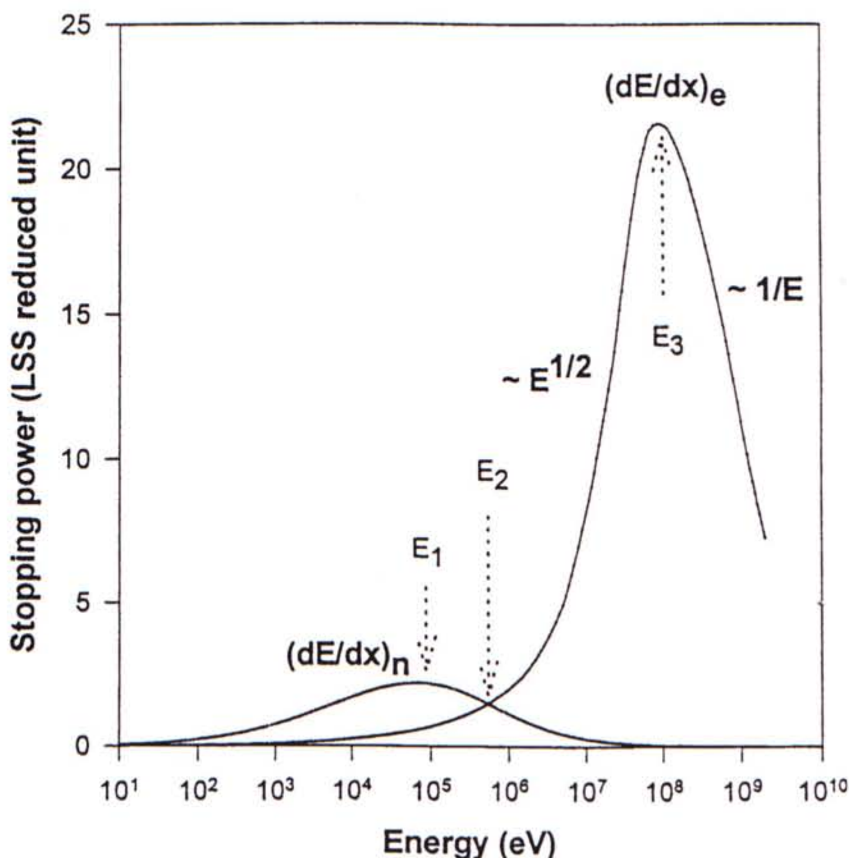

Fig. 2.2 Nuclear and electronic stopping power curve (After Feldman [5])

2.3. Kinematics of binary elastic collision

Nuclear stopping is caused by a collision between two atoms, and can be well described by classical kinematics. Consider the elastic head-on collision of two hard spheres shown in Fig. 2.3. For an incident sphere of mass M_1, value of velocity and energy are v and E_0, while the target sphere of mass M_2 is at rest. After the collision, the values of the velocities v_1 and v_2 and energies E_1 and E_2 of the projectile and target sphere are determined by the scattering angle θ and recoil angle ϕ. Applying the principles of conservation of energy (elastic collision) and conservation of momentum parallel and perpendicular to the direction of incidence:

$$\tfrac{1}{2}M_1v^2 = \tfrac{1}{2}M_1v_1^2 + \tfrac{1}{2}M_2v_2^2 \tag{2.2}$$

$$M_1v = M_1v_1\cos\theta + M_2v_2\cos\phi \tag{2.3}$$

$$0 = M_1v_1\sin\theta - M_2v_2\sin\phi \tag{2.4}$$

Solving the above equations, if $M_1<M_2$,

$$\frac{E_1}{E_0} = \left[\frac{\left(M_2^2 - M_1^2\sin^2\theta\right)^{1/2} + M_1\cos\theta}{M_2 + M_1}\right]^2 \tag{2.5}$$

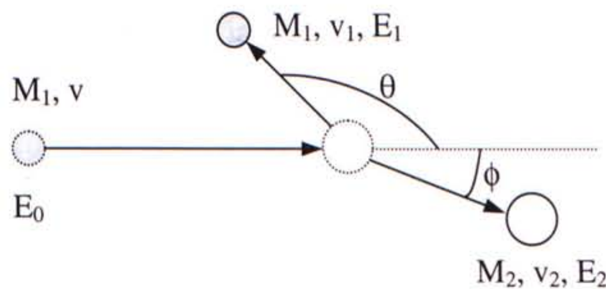

Fig. 2.3 Schematic of binary elastic collision (After Feldman [5])

If $M_1>M_2$, there is a critical angle θ_m representing the maximum angle through which M_1 can be scattered. θ_m is found by

$$\cos^2\theta_m = 1-\frac{M_2^2}{M_1^2}, \qquad 0\le\theta_m\le\frac{\pi}{2} \tag{2.6}$$

The energy ratio, is called the kinematic factor K. For $\theta=180°$, the energy E_2 transferred to the target sphere is maximum and given by,

$$\left.\frac{E_2}{E_0}\right|_{max} = \frac{4M_1M_2}{(M_1+M_2)^2} \tag{2.7}$$

Strictly speaking, for ion-solid interaction, the projectile is under electrostatic force from all the particles within the target solid. It will be a many-body interaction and too complicated to be considered. However, the many-body interaction can be simulated by considering the electrostatic force exists between the two colliding atoms, and restricting the electrostatic force to be a central force, e.g. coulombic potential multiplied by a screening function of r (radial axis). The equation of motions of the atoms can be integrated to yield the scattering angle θ for a given incident energy E and impact parameter b.

2.4. Nuclear and Electronic Stopping

The nuclear energy-loss rate is the energy lost by a projectile due to elastic collisions per unit length traveled in the target. The probability of a particle with energy E while traveling a distance dx, which results in an energy loss bewteen T and T+dT is given by

$$P(E,T)dT = Ndx\frac{d\sigma(E)}{dT}dT \tag{2.8}$$

where T is the transfer energy to the target atom, N is the atomic density, $d\sigma(E)/dT$ is the differential energy-transfer cross-section. The average energy loss is obtained by multiplying Eq. (2.8) by the transfer energy T and integrating over all possible values,

$$\langle dE \rangle = \int TP(E,T)dT = Ndx\int_{T_{\min}}^{T_{\max}} T\frac{d\sigma(E)}{dT}dT \qquad (2.9)$$

$$\left.\frac{dE}{dx}\right|_n = N\int_{T_{\min}}^{T_{\max}} Td\sigma(E) \qquad (2.10)$$

where T_{min} is the energy needed to displace an atom from its lattice site, approximately 20-30 eV. T_{max} equals E_2 in Eq. (2.7).

Electronic energy-loss is caused by interaction with the electrons of the target. Detailed modeling is very complex, but in the low-energy regime, the stopping is similar to a viscous drag force and is proportional to the ion velocity ν. Lindhard and Scharff [6] proposed the following expression,

$$\left.\frac{dE}{dx}\right|_e = \left[\frac{Z_1^{7/6}Z_2}{\left(Z_1^{2/3}+Z_2^{2/3}\right)^{3/2}}\right]8\pi a_0\hbar N\nu \qquad (2.11)$$

where a_0 is the Bohr radius. In the high energy regime, the energy-loss rate is given by the Bethe's formula [4].

2.5. Radiation Damage

When the projectile ion enters the target, it undergoes a series of collisions with the target atoms. In these collisions, if sufficient energy is transferred to the target atom, it will be displaced from its lattice position. This displacement threshold is called the displacement energy, E_d. If the transfer energy is less than E_d, the struck atom undergoes large amplitude vibrations without leaving its lattice position. The

transfer energy is quickly shared with nearest neighbours and dissipated as a localised source of heat. The displacement energy depends on the direction of the momentum of the target atom. The minimum displacement energy for germanium is 15 eV. The target atom that is displaced by the projectile is called primary knock-on atoms or PKAs. The PKAs can in turn displace other target atoms, secondary knock-on atoms, tertiary knock-on atoms, *etc*. This creates a cascade of atomic collisions as shown in Fig. 2.4. This leads to a distribution of vacancies, interstitial atoms, and other types of lattice disorder in the region around the ion track. As the number of ions incident in the crystal increases, the individual cascade begins to overlap. At some point, a heavily damaged layer is formed.

The average number of displaced atoms in a cascade produced by a PKA of energy E is denoted by $\langle N_d(E) \rangle$, the damage function. The simplest calculation of damage function is by the hard-sphere model of Kinchin and Pease (1995). By correctly accounting for electronic stopping and using a realistic interatomic potential, the Kinchin-Pease damage function is modified to

$$\langle N_d(E) \rangle = \begin{cases} 0 & (\text{for } 0 < E < E_d) \\ 1 & (\text{for } E_d \le E \le 2E_d/\xi) \\ \dfrac{\xi \nu(E)}{2E_d} & (\text{for } 2Ed/\xi \le E < \infty) \end{cases} \qquad (2.12)$$

where ν(E) is the amount of PKA energy not lost to electronic excitation and both analytical theory and computer simulation suggest a value ξ near 0.8.

Fig. 2.4 Schematic of the formation of collision cascade by a PKA

2.6. Spikes

In the last section, how a collision cascade created by a PKA is described. What happens if there is a cascade, which is of extra high density? A spike may appear. It is a high-density cascade that possesses a limited volume in which the majority of atoms are temporary in motion. Define λ_d, the mean free path, be the average distance travelled by an energetic particle between displacement collisions with target atoms. The probability of a projectile with energy E collide with a target atom, transferring an energy greater than the displacement energy while traversing a thickness dx, is given by,

$$P(E) = N\sigma(E)dx \tag{2.13}$$

where N is the target atomic density, σ(E) is the total collision cross-section. Putting P(E)=1, dx replaced by λ_d, we get

$$\lambda_d = \frac{1}{N\sigma(E)} \tag{2.14}$$

In intermediate energy regime and using power law approximation, $\lambda_d \propto E^{1/2}$.

Therefore if the projectile energy decreases, the distance between collisions becomes less, until λ_d approaches the interatomic distance of the target atoms. That means a new PKA is created at every lattice site along the ion trajectory. Now the cascade can no longer be thought of as a collection of isolated vacancy and interstitial point defects, but looks like a volume of material which is composed of a core of vacancies surrounded by a shell of interstitial atoms (Fig. 2.5). It is generally referred to as a displacement spike. It takes ~10^{-13} s to form, of the order of a lattice vibration time.

When the displacement spike ends, all the displaced atoms have insufficient energy to cause further displacement. Energy will be shared with the nearest neighbours and dissipated as heat. After approximately 10^{-12} s, a state of dynamic equilibrium may result and the vibration energy approximates a Maxwell-Boltzmann distribution. Such period of lattice heating is referred as the thermal spike phase of the collision cascade. For a Maxwell-Boltzmann distribution of heat, the temperature is related to the mean deposited energy density $<\theta_d>$ by,

$$\langle \theta_d \rangle = \frac{3}{2} k_B T \tag{2.15}$$

where k_B is Boltzmann's constant.

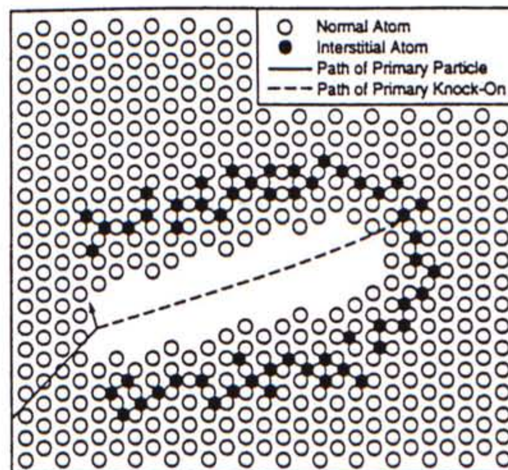

Fig. 2.5 Schematic of a displacement spike (After Nastasi, 1996)

2.7. Topography of Ion Bombarded Surface

As a conclusion of the previous sections, we start by introducing the general concept of what would happen if a projectile bombards a target. The origins of the energy-loss are presented. Before we go deeper to look into the nuclear stopping, we discuss the kinematics of binary elastic collision, which can demonstrate how the nuclear elastic collision can be considered in a simplified way. Then we introduce the concept of probability of scattering, which by integration can obtain the average energy-loss by nuclear scattering when the projectile travels a distance dx. The formula to calculate electronic energy-loss in the low-energy regime is also presented. After considering the fate of the projectile, we look into the target and discuss the origin of the collision cascade, and the formula to calculate the average number of atoms displaced by one PKA. In reality, we should consider the cumulative effects of many PKAs of different energies. When we consider the spatial distribution of point defects as the PKA slows down and comes to rest, it leads to the concept of a spike, including the displacement spike and the thermal spike.

After all these discussions, we are now in a position to climb up and have a bigger picture about the implantation process. How would the implantation modify the surface topography of a solid?

To answer this question, we start from considering what atom fluxes are going into and out of an element of the solid surface. A more detailed discussion can be found in a review paper by Professor Wilson [7]. The various atom fluxes are shown in Fig. 2.6.

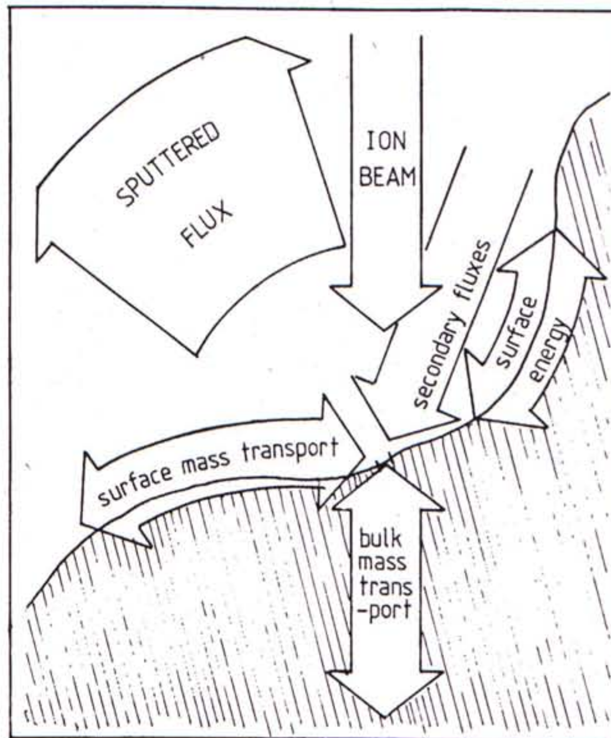

Fig. 2.6 Atom fluxes into and out of an element of solid surface under the action of an ion beam (After Wilson, 1989)

(a) The incident ion beam – generally the ion beam is not uniform, and has an imperfect collimation, $\Delta\theta$, and spatial non-uniformity, Δx. Imperfect collimation will affect the sputtering yield, S, at different area of the surface as sputtering yield depends very much on the incident angle. Spatial non-uniformity will contribute to non-uniform sputtering, as the incident fluxes are different at different area. The projectiles will create collision cascade or even spike inside the solid, which may generate craters on the surface as a result of surface relaxation due to lattice stress created by segregation of the point defects in the cascade.

(b) The sputtered flux – the treatment of many ion-bombardment-induced surface erosions is based on the angular variation of sputtering. Sputtering is the removal

of the near-surface atoms from the target by energetic particle bombardment. There are two types of sputtering, physical sputtering and chemical sputtering. The former describes the transfer of kinetic energy from the projectile to the target atoms, which results in the ejection of atoms out of the target surface. The latter is the implantation of an active atom, which lowers the surface binding energy of the target and result in a dramatic increase in the sputtering yield. Sputtering yield, S, is defined as the average number of sputtered target atoms per incident atom. It has been predicted by Sigmund theory [8] on the basis of nuclear energy mechanisms and the sharing of energy loss among the large number of atoms, which are involved in the collision cascade. The Sigmund theory also predicts the change of the sputtering yield as a function of the angle of incidence, θ. When θ increases, there is a greater chance that the cascade is close to the surface, and more energy is deposited near the surface, therefore the sputtering yield increases. At very high incident angle, projectiles may get reflected from the target surface, as the momentum normal to the surface is not great enough to penetrate the surface barrier. Therefore less energy is deposited on the surface and the sputtering yield decreases. The sputtering yield thus attends a peak at $\theta_c = 60° \sim 80°$. Because of anisotropy and channelling in a single crystal, sputtering yield may attend more than one local peak for θ scanning through 0° to 90° and may not increase monotonically. Stewart and Thompson [9] suggested a simple 2-dimensional model to consider the movement of inclined planes and their point of intersection under the sputtering effect of ion beam. Assuming a smooth $S(\theta)$ with one peak, θ_c, and ignoring redeposition effect (to be discussed), ion beam bombards the inclined planes as

shown in Fig. 2.7 in normal incidence. In Fig. 2.7(a), for $\theta < \theta_c$, d' > d as $S(\theta) > S(0°)$, more target atoms are sputtered out from the inclined plane, and the inclined plane will apparently move towards the elevated side. However, in Fig 2.7(b), quite different situation arises because at the upper corner, a microscopically small area must have the most favourable attack angle θ_c, this gradually widens as it gets the highest sputtering yield until the whole slope has changed to θ_c.

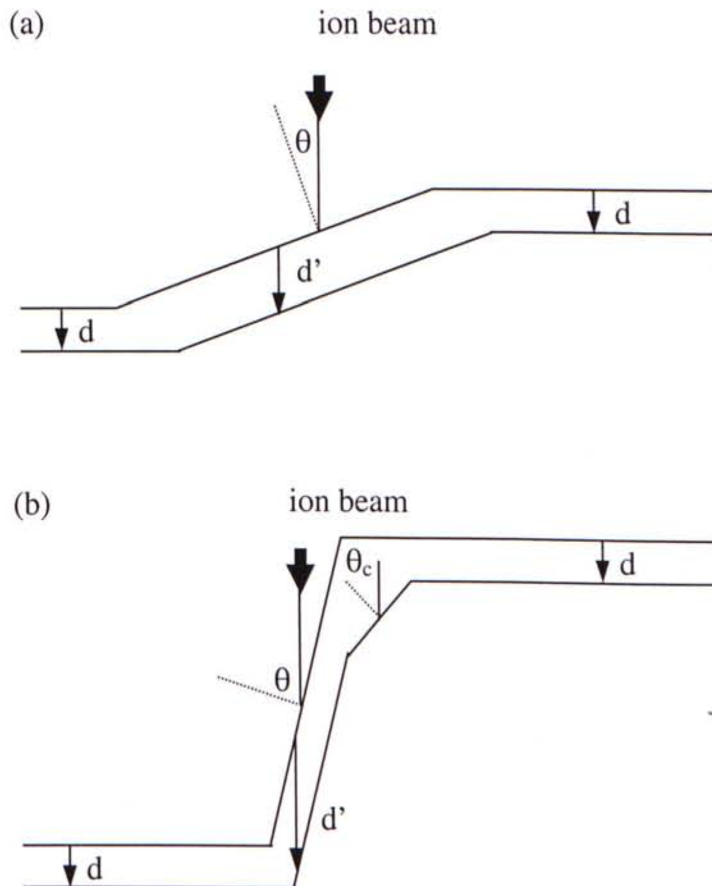

Fig. 2.7 Schematic of the evolution of inclined planes under the action of an ion beam, (a) $\theta < \theta_c$, (b) $\theta > \theta_c$ (After Wilson, 1989)

(c) Secondary fluxes – these can be subdivided into two types, including primary ion reflection and sputtered atoms. The former occurs when the reflected ions lose little energy and add to the erosion caused by the primary ion beam. The latter is the sputtering created by the sputtered atoms. In general, the average energy of the sputtered atoms is ~10 eV so too small to sputter the other atoms but their energy imparts high sticking probability.

(d) Surface mass transport – the driving forces of surface atom transport are mainly concentration gradient and chemical potentials. The former tends to produce a more homogeneous surface. The latter leads to segregation, such as nucleation and growth of a new phase.

(e) Surface energy – a third driving force for transportation, which occurs to minimise surface energy by minimising surface area.

(f) Bulk mass transport – large point defects fluxes are created by ion bombardment. These can lead to segregation and alters the surface binding energy. Voids may be formed when the collision cascade density is very high.

CHAPTER 3 EQUIPMENT REVIEWS

This Chapter serves as a brief introduction to the equipment and characterisation methods used throughout the research. The mechanism, advantages and limitations for each equipment will be briefly discussed. Detailed discussion about the theoretical mechanism and applications can be found in the references suggested in each session.

3.1. Metal Vapour Vacuum Arc Ion Source Implanter (MEVVA)

Ion implantation process is briefly described in Chapter 1. There are many types of ion sources, such as hot-cathode, cold-cathode, high frequency, duoplamatron and sputter sources. The ion source being used in our laboratory, the metal vapour vacuum arc ion source, was first developed by Brown *et al* in Lawrence Berkeley Laboratory in 1985 [43].

A schematic of the MEVVA ion source electrical configuration used in our laboratory is shown in Fig. 3.1. The projectile material is put as the cathode. A small motor drive is used to push the cathode forward at a constant step so as to compensate the material loss during implantation. Therefore a constant flux can be maintained. The main arc is initiated by a trigger spark discharge between the cathode and the trigger electrode. The trigger voltage is in the form of a voltage pulse with a fixed width of 1.2 ms, around 5 – 10 kV, at a variable frequency ranging from 1 – 25 Hz. Because of the high voltage pulse, cathode spots are formed on the cathode surface, with a current density of rough order 10^6 A cm^{-2}, serving to vaporise and ionise the cathode material within the spots [58].

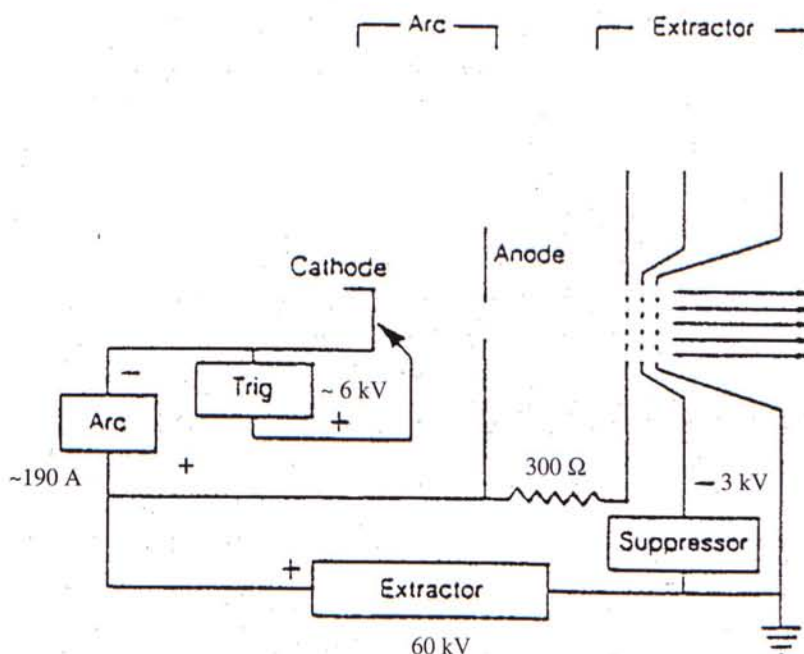

Fig. 3.1 Schematic of the source electrical configuration
(After I. G. Brown [58])

The cathode spots act as regions of plasma generation from the solid surface. This quasi-neutral plasma plumes away from the cathode toward the anode, and thus completes the electrical circuit. The detailed process involved in the breakdown and plasma growth of the metal vapour vacuum arc discharge has not yet been fully understood.

The positive ions within the plasma are then accelerated by the electric field produced by the extractor voltage, 60 kV. Ions produced are multiply ionised, thus contributing to different charge states for different elements. A suppresser voltage, about –3 kV, is applied to prevents the flow of secondary electrons, created by the ion beam bombarded onto the target surface, back across the gap and contributing to the load of the extractor power supply.

The implanting dose is determined by the time of implantation and the trigger frequency. The higher the trigger frequency, the larger is the mean current density as well as the dose. The target sample is put on a stainless steel holder with oil coiling at the back. Temperature is monitored by a thermocouple touching the surface of the sample. The temperature is also affected by the time of implantation and the trigger frequency.

MEVVA ion source implanter is useful as high beam current density is readily extracted from the ion source. In the case of forming a buried layer of the projectile compound, high dose ion implantation (~10^{17} ions cm^{-2}) is required. This implies an implantation time of weeks or even months for conventional implanter, comparing to half-day work by using MEVVA ion source implanter.

However, some limitations also exist. Multiple charge states are usually created in the stage of plasma formation. This can complicate the experiment, as different charges will possess different energy, say at an extraction voltage of 60 kV, Co^+ ions possess 60 keV, Co^{2+} ions possess 120 keV. Another problem arises in temperature measurement. The thermocouple itself is under constant implantation and thus its properties keep changing. Moreover, the thermocouple measures the average temperature over the whole sample, but not the instantaneous temperature under the beam spot. Wittkower [60] suggested a formula to calculate the instantaneous temperature rise under the beam spot:

$$T(s,t) - T(s) = \frac{2J_i \cos\theta}{k} \sqrt{\frac{kt}{\rho C_p}} \tag{3.1}$$

where

T(s,t) = the "instantaneous" temperature of the sample surface under the beam spot (°C)

$T(s)$ = the average temperature (°C)

J_i = the "instantaneous" power density of the ion beam (W cm^{-2})

ρ = the density of the sample (gm cm^{-3})

C_p = the specific heat (W s / gm °C)

t = the length of time the beam strikes that spot on the surface (s)

D. H. Zhu [61] suggested performing computer simulation to calculate the instantaneous temperature by considering the thermal conduction equations. More detailed discussion on the MEVVA ion source implanter can be found in the listed review papers [62-70].

3.2. Atomic Force Microscopy (AFM)

The AFM provides the ability to acquire three-dimensional data with angstrom resolution from conducting to non-conducting surfaces. Operationally, the AFM relies on a piezoelectric tube scanner to produce a precise scan in the X-Y plan with a lateral resolution of about 1 nm, while feedback is used to control the contact force of a very sharp probe on the surface of the sample. The very sharp tip used for the AFM probe is on the end of a flexible cantilever. Features on the sample cause the cantilever to deflect as the sample moves under the tip. An optical sensing system as shown in Fig. 3.2 monitors the deflection of the cantilever. The beam reflects off the back of the cantilever onto a split photodiode. The differential signal from the split photodiode provides a sensitive measure of the cantilever deflection. The feedback signal controls the height of the piezoelectric scanner as the sample is scanned. The height of the piezoelectric scanner relates directly to the topography of the sample surface with a displacement as small as 10 Å.

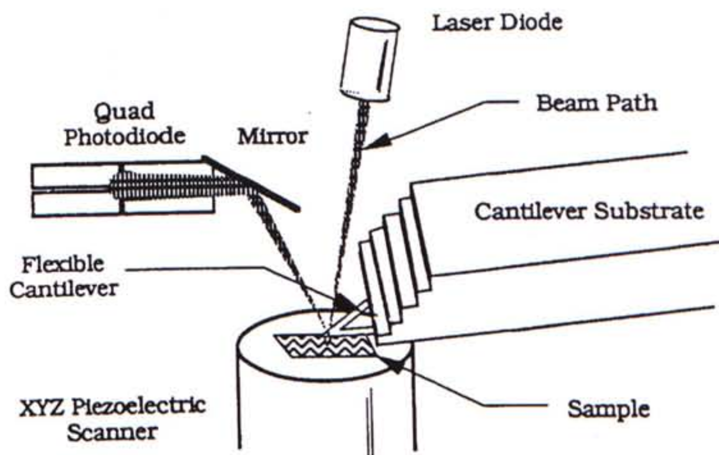

Fig. 3.2 AFM optical sensing system (After MultimodeTM SPM Instruction Manual, Digital Instruments)

Several forces typically contribute to the deflection of an AFM cantilever. The force most commonly associated with AFM is an interatomic force, the van der Waals force. The dependence of the van del Waals force upon the distance between the tip and the sample is shown in Fig. 3.3. Two distance regimes are labelled: a) the contact regime; and b) the non-contact regime.

In the contact regime, the cantilever is held less than a few angstroms from the sample surface, and the interatomic force between the cantilever and the sample is repulsive. In addition to the repulsive van der Waals force, a capillary force exerted by the thin water layer often present in an ambient environment, and the force exerted by the cantilever itself are also presented. The total force that the tips exerts on the sample is the sum of the capillary plus cantilever forces, and must be balanced by the repulsive van del Waals force for contact AFM. The magnitude of the total force exerted on the sample varies from 10^{-8} N to the more typical operating range of 10^{-7} to 10^{-6} N.

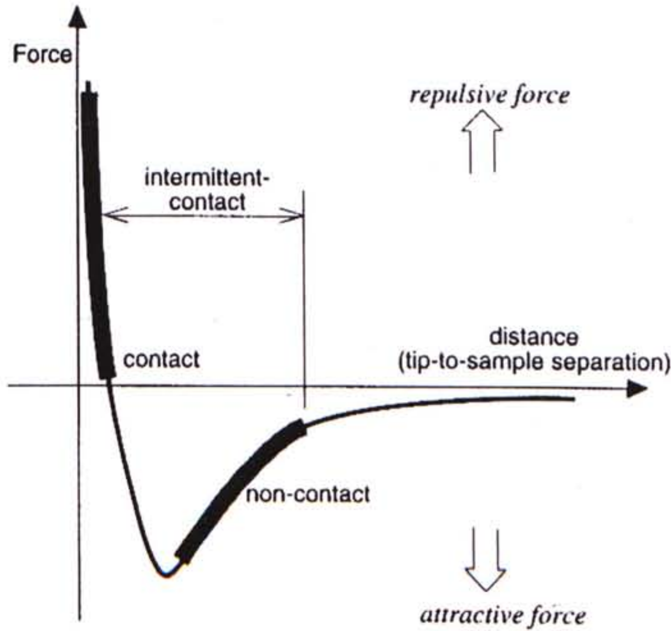

Fig. 3.3 Interatomic force vs. distance curve (After Introduction to SPM, Park Scientific Instruments)

In non-contact mode, or what we call the tapping mode, the spacing between the tip and the sample is on the order of tens to hundreds of angstroms. The total force between the tip and the sample is very low, generally about 10^{-12} N. In tapping mode, the system vibrates a stiff cantilever near its resonant frequency (typically from 100 to 400 kHz) with an amplitude of a few tens to hundreds of angstroms. The force gradient, which is the derivative of the force versus distance curve shown in Fig. 3.3, changes with tip-to-sample separation. The force gradient, $\partial F_Z / \partial Z$, acts to modify the effective spring constant k of the cantilever according to $k = k_o + \partial F_Z / \partial Z$, where k_o is the spring constant of an isolated cantilever. The resonant frequency of the cantilever varies as the square root of its spring constant. Therefore, changes in the root mean square (RMS) amplitude, phase or frequency of the cantilever vibration can be used to reflect the changes in the tip-to-sample spacing, hence sample topography.

AFM has many advantages comparing to the conventional optical microscopy, SEM or TEM [71]: little or no sample preparation; non-destructive in nature; high flexibility in types of samples: insulators, semiconductors, and conductors, transparent as well as opaque materials; high flexibility in operating environment: in air, in liquid, in ultra-high vacuum, and at various temperatures; three-dimensional quantitative nature of topographical data.

However, AFM also suffers from several limitations. One of these limitations is its inability to distinguish among different atomic species. Another one is that the topography measured reveals information about the vertical height of the sample surface as well as some characteristics of the sample material itself. These material characteristics include the rigidity, elasticity, and friction of the sample surface. Moreover, AFM images are subject to some artifacts, known as tip convolution or tip imaging. It means that every data point in an image represent a convolution of the shape of the tip and the feature on the sample surface. The larger the tip size relative to the surface feature of the sample, the larger the image distortion can be. More detailed discussion about the theory and applications of AFM can be found in the listed references [72-75].

3.3. Rutherford Backscattering Spectrometry (RBS)

Backscattering spectrometry using ion beams with energies in the MeV range has been used extensively for accurate determination of stoichiometry, areal density and depth profile of impurities. Measurement of the number and energy distribution of ions backscattered from atoms in the near surface region of target materials allows identification of the atomic species and determination of the distribution as a function of depth.

Application of RBS to thin film analysis is illustrated in Fig. 3.4 for the ideal case of a two-element (elements A and B) thin film of uniform composition (A_mB_n throughout the whole layer of thin film) on a low mass substrate. Projectiles, typically $^4He^{2+}$, enter the surface of the target material, lose energy due to inelastic electron stopping (refer to section 2.2), until they collide with the target atoms elastically. After they have transferred part of their energy to the target atoms, they are backscattered and lose energy again in the outward path due to inelastic electron stopping. Energy analysis of the backscattered projectiles by the detection system yields the backscattering spectrum displayed in the lower portion of Fig. 3.4 in the form of counts per channel vs. channel number. The channel number is normally linearly related to the backscattered ion energy, E_1. Appearing in the spectrum is a nearly flat-topped peak for each element present in the film. The peak widths are caused by the energy loss of the projectiles in the target material.

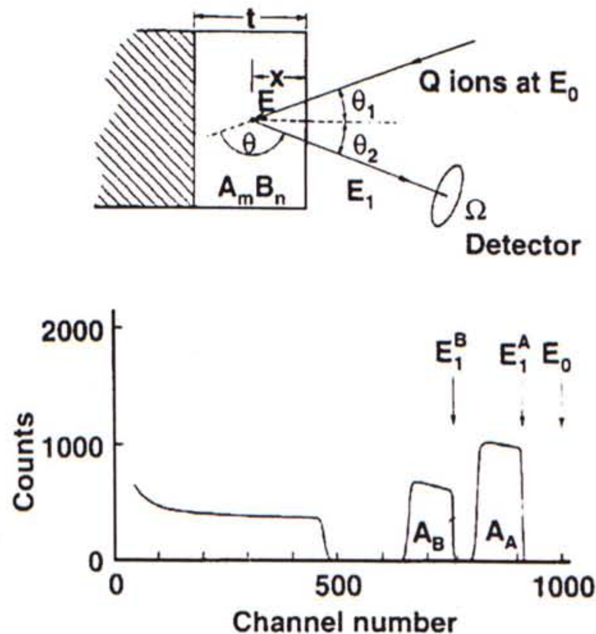

Fig. 3.4 Basic backscattering spectrometry. Experimental geometry (upper figure); Backscattering spectrum (lower figure) (After Handbook of Modern Ion Beam Materials Analysis [76])

The film elements may be identified by measuring the energy at the high-energy edge ($E^A{}_1$ and $E^B{}_1$) of each peak. Referring to Eqn. (2.5),

$$K = \frac{E_1}{E_0} = \left[\frac{\left(M_2^2 - M_1^2 \sin^2\theta\right)^{1/2} + M_1 \cos\theta}{M_2 + M_1} \right]^2 \tag{2.5}$$

where M_1, M_2 are the masses of the projectile atom and target atom respectively. E_0 and E_1 are the energies of the projectile before and after collision respectively. θ is the scattering angle. Substituting $E^A{}_1$ and $E^B{}_1$ into E_1, K_A and K_B can be found, as well as M_A and M_B as θ is fixed for a given geometry. Energy loss in the inward and outward paths is not taken into account, as the counts in the high-energy edge correspond to backscatterings at the surface of the target material only.

The areal density, (Nt), in atoms per unit area, may be determined for each element from knowledge of the detector solid angle Ω, the integrated peak count A for Q incident projectiles, and the measured or calculated cross section $\sigma(E,\theta)$ using

$$Nt = \frac{A\cos\theta}{Q\Omega\sigma(E,\theta)} \tag{3.2}$$

where N is the atomic density (atoms per unit volume) and t is the physical film thickness. Cross section is defined by the probability of an incident projectile being backscattered per unit detector solid angle, per unit of areal density of target material. Let $M_{AB} = mM_A + nM_B$ be the molecular weight of the compound A_mB_n, ρ_{AB} be the film density, the number of atoms A and B per unit compound volume, N_A and N_B respectively, are given by:

$$N_A = \frac{m\rho_{AB} N_o}{M_{AB}} \quad ; \quad N_B = \frac{n\rho_{AB} N_o}{M_{AB}} \tag{3.3}$$

where N_0 is Avogadro's number.

The thickness t is calculated by:

$$t = \frac{(Nt)_A}{N_A} = \frac{(Nt)_B}{N_B} \tag{3.4}$$

The average stoichiometric ratio for the compound may be calculated from Eqn. (3.3):

$$\frac{n}{m} = \frac{N_B}{N_A} = \frac{A_B \sigma_A(E,\theta)}{A_A \sigma_B(E,\theta)} \tag{3.5}$$

The principal strengths of RBS are: (a) it is an absolute method that does not require the use of standards; (b) it is quick and easy; (c) it is frequently non-destructive; (d) it may be used for depth profiling (with 10-30 nm depth resolution).

The technique's principal weakness is that it is not good for trace-element analysis. It has very poor sensitivity to light elements in or on heavy matrices, also it is theoretically impossible to separate the signals coming from two elements with similar mass and present in similar depth. More detailed discussion of RBS can be found in the listed references [4,5,76].

3.4. X-ray Diffraction (XRD)

X-rays are electromagnetic radiation of exactly the same nature as light but of very much shorter wavelength (X-rays: 0.5 – 2.5 Å; visible light: 6000 Å). X-ray are produced when any electrically charged particle of sufficient kinetic energy is rapidly decelerated. Therefore, when an X-ray beam encounters any electron, the electron will be set into oscillatory motion about its mean position. Then the accelerating or decelerating electron emits another electromagnetic wave. In this sense, an electron is said to scatter x-rays, whereas the scattered beam is simply the beam radiated by the electron under the action of the incident beam. For an atom, the scattered beam is

the vector sum of the scattered beams of its electrons. Normally, the x-rays are scattered in all directions.

Consider the case when an x-ray is scattered by a crystal [77]. Fig. 3.5 shows a section of a crystal, its atoms arranged on a set of parallel planes A, B, C, D… and spaced a distance d' apart. Assume a beam of perfectly parallel, perfectly monochromatic x-ray of wavelength λ is incident on this crystal at an angle θ. Rays 1 and 1a strike atoms K and P in the first plane of atoms respectively, and are scattered in all directions. Only in the direction 1' and 1a' are these scattered beams completely in phase and reinforce each other. It is because the difference in their path lengths:

$$QK - PR = PK\cos\theta - PK\cos\theta = 0 \quad (3.6)$$

Similar, the rays scattered by all the atoms in the same plane in the direction parallel to 1' are in phase. This is true for all planes separately. For rays 1 and 2, scattered at atoms K and L, the path difference for rays 1K1', 2L2':

$$ML + LN = d'\sin\theta + d'\sin\theta = 2d'\sin\theta \quad (3.7)$$

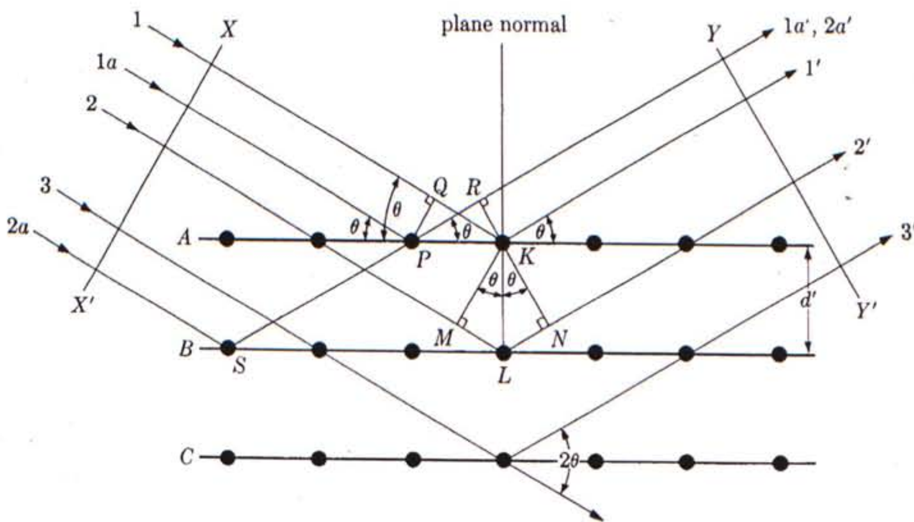

Fig. 3.5 Diffraction of x-rays by a crystal
(After Cullity [77])

Scattered rays 1' and 2' will be completely in phase if

$$n\lambda = 2d'\sin\theta \tag{3.8}$$

This is true for all other pairs of adjacent planes. Eqn (3.8) states the essential condition, which must be met if constructive interference for the adjacent planes is to occur. Therefore, for fixed value of λ and d', there may be several angles of incidence θ_1, θ_2, θ_3... corresponding to n =1, 2, 3...

As a result, by tabulating all these angles and scan through them, d' can be accurately determined. The unknown crystal under investigation can thus be identified.

X-ray diffraction is non-destructive in nature. Besides chemical identification, particle size of very small crystals can also be obtained by measuring the width of their diffraction curves and calculated by Scherrer formula. The x-ray diffraction can also be used to find the stress, texture or quality of the crystal.

CHAPTER 4

STUDY OF ION BEAM IMPLANTED GERMANIUM BY ATOMIC FORCE MICROSCOPY AND RUTHERFORD BACKSCATTERING SPECTROMETRY

4.1. Introduction

Ion bombardment of solids leads to dramatic and various changes in surface morphology. Current understanding of the origin and evolution of these surface structures is far from being complete [7]. Besides its own scientific interest in this subject, it finds great technological importance in a number of contemporary industrial applications and particularly in microelectronics where element dimensions are continuously decreasing, and hence, geometry and precision requirements become increasingly stringent.

Dating back to 1968, Parsons and Hoelke [10] has studied the features of the damaged layer caused by 100 keV O^- ion implantation into Ge using ion channelling and transmission electron microscopy (TEM). Since about 1975, there has been an increasing interest in using these two techniques to obtain information about the damaged region produced in individual cascades in Si and Ge [11-14].

In 1982, Professor Wilson studied the surface topography of self-ion bombarded single-crystal germanium by high-resolution scanning electron microscopy (SEM) [15]. He observed holes with 400 Å mean separation appeared at doses above 2×10^{15} ions cm^{-2} (ion energy 50 keV). These holes enlarged with increasing dose and developed into a complex cellular structure. Starting from 1982 to 1985, Appleton *et al.* [16-18] using cross-sectional TEM, found that heavy ion

irradiation created a morphological instability in the amorphous Ge which erupted to form surface craters or columnar voids of 200-400 Å in diameter, causing a large expansion of the amorphous layer.

The development of scanning tunnelling microscopy (STM) has brought about a unique opportunity to examine ion-bombardment-induced surface morphology on a nanometer scale. In 1985, Feenstra and Oehrlein [19] reported a STM study in high dose Ar-implanted Si. In 1988, Professor Wilson *et al.* [20-21], presented the first observation of single ion impact on SiO_2 / Si interfaces and galena (PbS) by STM. Overlap of collision cascades were avoided by using low dose implantation (~10^{11} ions cm^{-2}). They suggested that surface topography in the form of craters be related to the cascade damage rather than to the removal of atoms by sputtering. In 1989, Porte *et al.* [22] used air STM to observe single ion impact on highly oriented pyroletic graphite (HOPG) surfaces. With the rapid development of STM and related techniques in the last decade, various solid surfaces including metal, semiconductors, bombarded by different ions at a wide range of energies, doses, incidence angles and temperatures have been studied by scanning probe microscopy (SPM) [23-25].

In our laboratory, Dr. Y. J. Chen, had carried on the study of ion-bombardment-induced surface morphology by STM and atomic force microscopy (AFM) [26-29]. Very flat $In_{0.22}Ga_{0.78}As$ layers on GaAs(100) surfaces were bombarded with low dose (10^{11} ions cm^{-2}) As^+ and B^+ ions at 35 keV. AFM revealed craters with average diameters of 14.6nm and 11.4nm for As^+ and B^+ respectively [26]. He also irradiated HOPG surfaces by 1.8 MeV electrons and found out that for near grazing incidence with a dose of 5×10^{12} e^- cm^{-2}, nm-hillocks were observed, being attributed to the effects of single electron-carbon interactions in the top surface

layers [27]. Another research done by Chen was implantation into Ge [28-29]. Epi-ready Ge(111) surfaces were implanted with Co ions to doses of 10^{16} to 5×10^{17} ions c^{-2} at accelerating voltage of 40-70 kV. Cellular nanostructures were observed by AFM. The variation of the root-mean-square roughness with ion dose, accelerating voltage, and mean beam current density was presented.

In this chapter, we report the study of ion-bombardment-induced damage and morphological development of germanium by Co-ion, C-ion and self-ion implantation using atomic force microscopy (AFM), and Rutherford backscattering spectroscopy (RBS).

4.2. Experiments

Chemomechanically polished n-type Ge(100) wafers with resistivity being less than 0.4 Ω-cm were used. The samples were loaded on a stainless steel sample holder with oil cooling and the temperature is monitored by a thermocouple. The implantation was carried out in a JYZ-8010W MEVVA ion source implanter in normal incidence operating at an extraction voltage of 60kV, ion doses ranging from 6×10^{14} to 6×10^{17} ions cm^{-2}. The implanter was operated in pulse mode with mean current density being 15 μA cm^{-2}. Because of the multiple charges nature of MEVVA, the particle flux corresponded to 34% Co^{+}, 59% Co^{2+} and 7% Co^{3+} for Co-ion implantation, 100% C^{+} for C-ion implantation, 60% Ge^{+} and 40% Ge^{2+} for self-ion implantation [30]. The maximum temperature recorded by the thermocouple and the implantation time for each sample are shown in Table 4.1.

The AFM observations were made in air at room temperature by Digital Instruments Nanoscope III, operating in the tapping mode. A slope correction to

Table 4.1 Summary of temperature and implantation time of the Co-ion, C-ion and self-ion as-implanted Ge samples

Bombarding ion	Dose /ions cm^{-2}	Max. Temp /°C	Implant. Time/min
Co	6×10^{14}	36	<1
	1×10^{15}	53	<1
	6×10^{15}	53	1
	1×10^{16}	60	2
	6×10^{16}	98	13
	1×10^{17}	105	38
	6×10^{17}	110	289
C	1×10^{15}	37	<1
	6×10^{15}	39	1
	1×10^{16}	40	2
	6×10^{16}	65	15
	1×10^{17}	90	45
	6×10^{17}	105	315
Ge	1×10^{15}	35	<1
	6×10^{15}	45	2
	1×10^{16}	77	2
	6×10^{16}	73	25
	1×10^{17}	100	48
	1.8×10^{17}	130	75

compensate for tilt of the sample relative to the scanning plane was performed by offline fitting a first order polynomial to the image and then subtracted it from the image. The image was flattened further using a third order planefit to compensate for the bowing of the piezo tube.

RBS random spectra with samples tilted at 7° and ion channelling spectra were obtained by HV Tandetron Accelerator at a 170° scattering angle with 2.0 MeV $^{4}He^{2+}$ particles.

4.3. Results and Discussion

4.3.1. AFM

Figure 4.1, 4.2 and 4.3 show the tapping mode AFM micrographs of the Co-ion, C-ion and self-ion implanted Ge with different doses respectively. Note that the scan area of Figure 4.1(a) to (c) is 800nm × 800nm, Figure 4.1(d) is 3μm × 3μm, Figure 4.1(e) is 5μm × 5μm, and Figure 4.1(f) is 15μm × 15μm, in order to view the overall structure more clearly. The scan area of Figure 4.2 is 400nm × 400nm, that of Figure 4.3 is 800nm × 800nm.

For Co-ion implanted Ge samples, cellular nanostructures are seen starting from a dose of 1×10^{15} up to 1×10^{16} ions cm^{-2} (Fig. 4.1(a), (b) and (c)). The craters increase in diameter and in depth with increasing dose. The mean values of the crater diameters and their standard deviations at various doses are given in Table 4.2. Each value is calculated by counting more than 100 craters. For doses higher than 1×10^{16} ions cm^{-2}, craters are in irregular shape instead of circular, therefore the mean diameter is not presented. The large standard deviation results from the statistical nature of the collision process.

Fig. 4.1 Tapping mode AFM micrographs of Co-ion implanted Ge at a dose of

(a) 1×10^{15} ions cm^{-2}

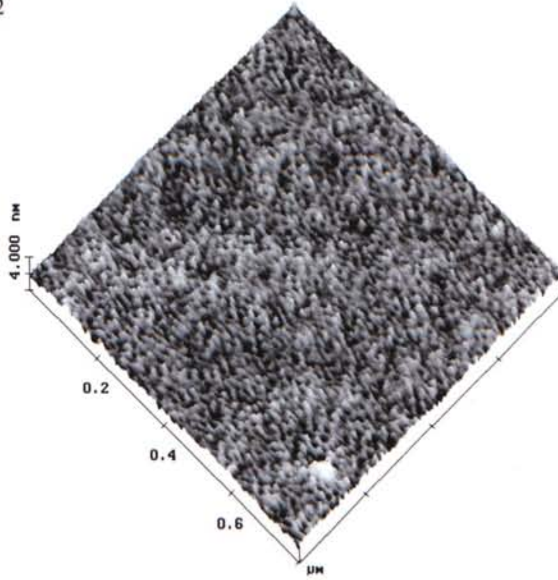

(b) 6×10^{15} ions cm^{-2}

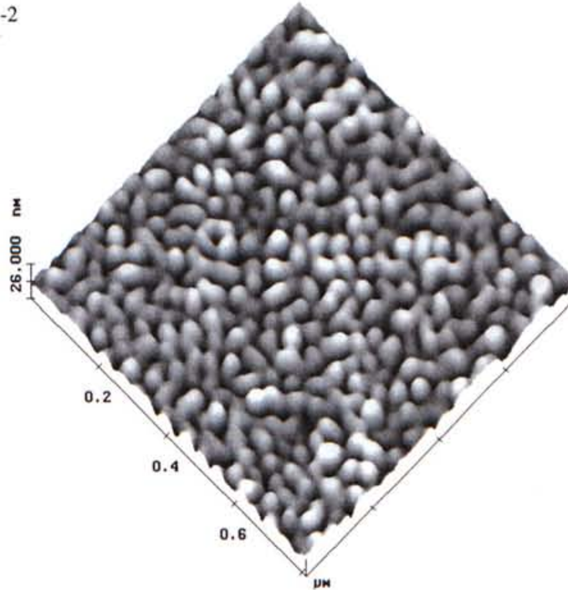

(c) 1×10^{16} ions cm^{-2}

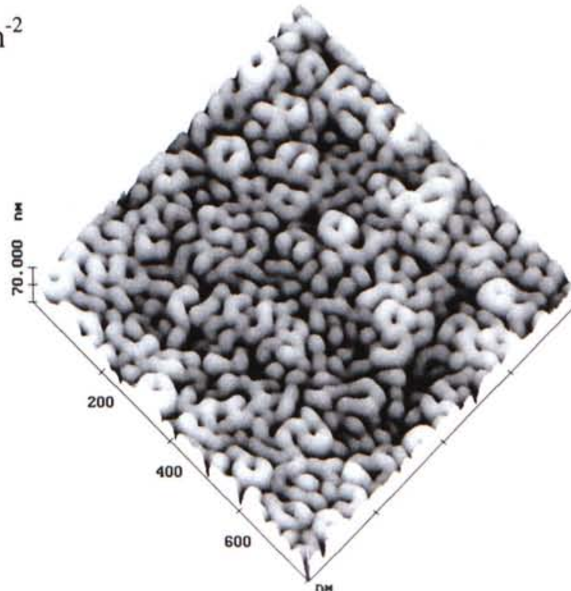

(d) 6×10^{16} ions cm^{-2}

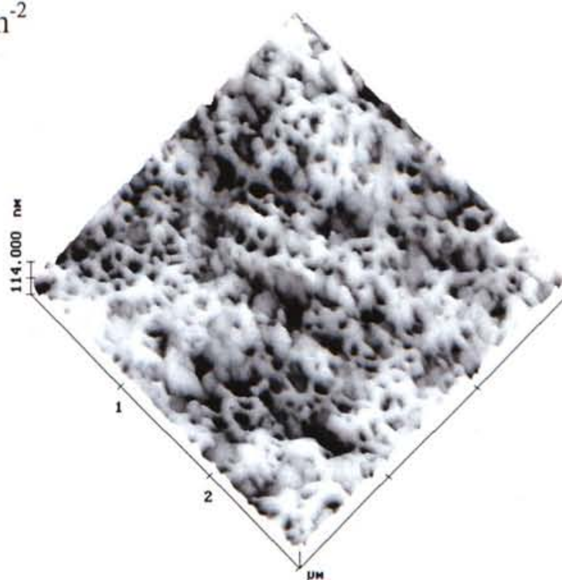

(e) 1×10^{17} ions cm^{-2}

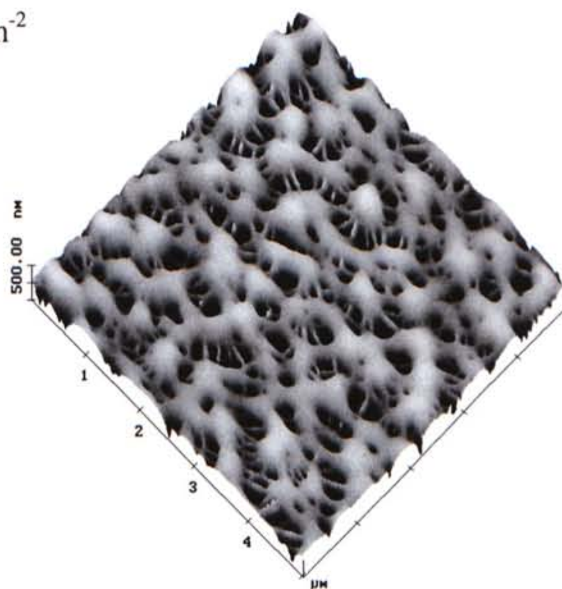

(f) 6×10^{17} ions cm^{-2}

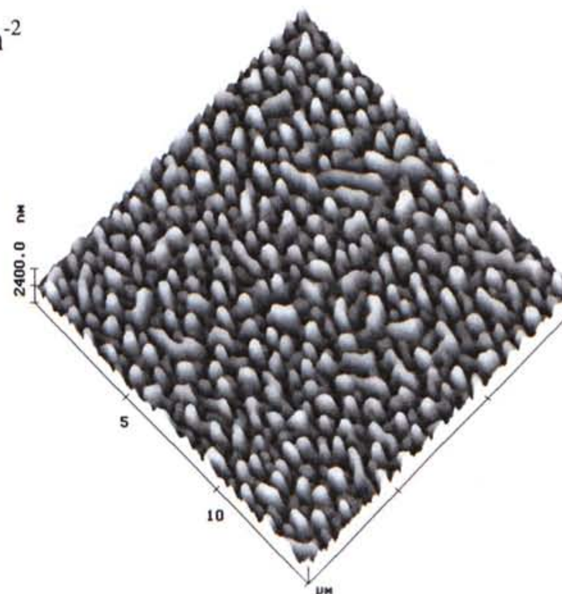

Fig. 4.2 Tapping mode AFM micrographs of C-ion implanted Ge at a dose of

(a) 1×10^{15} ions cm^{-2}

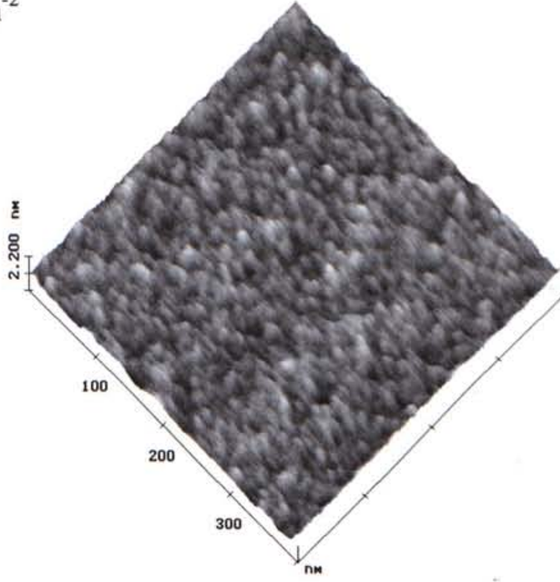

(b) 1×10^{16} ions cm^{-2}

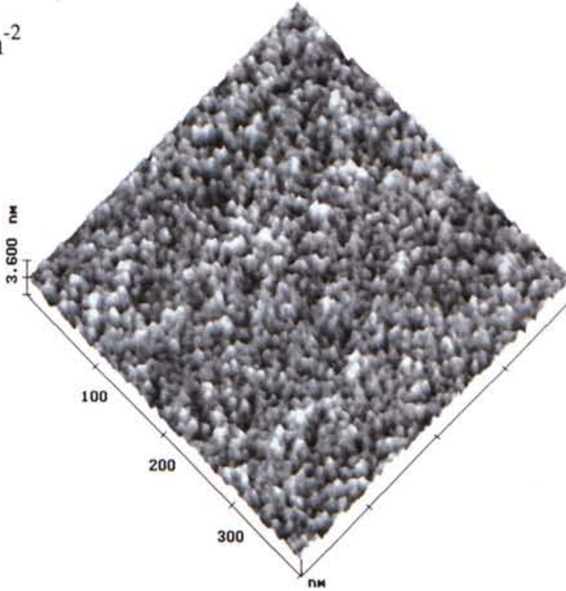

(c) 1×10^{17} ions cm^{-2}

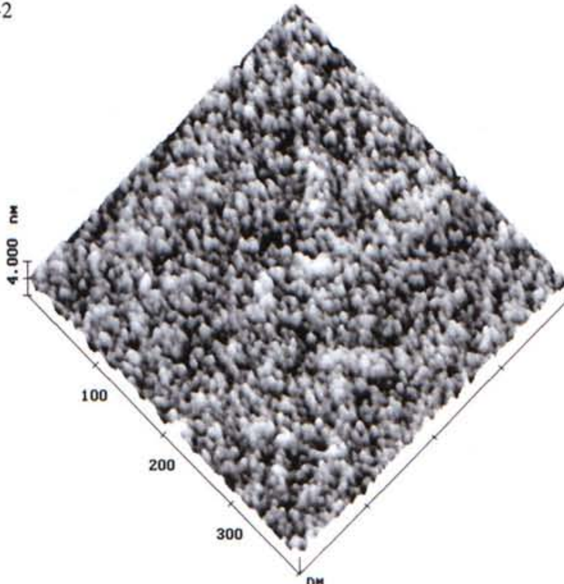

Fig. 4.3 Tapping mode AFM micrographs of self-ion implanted Ge at a dose of

(a) 1×10^{15} ions cm^{-2}

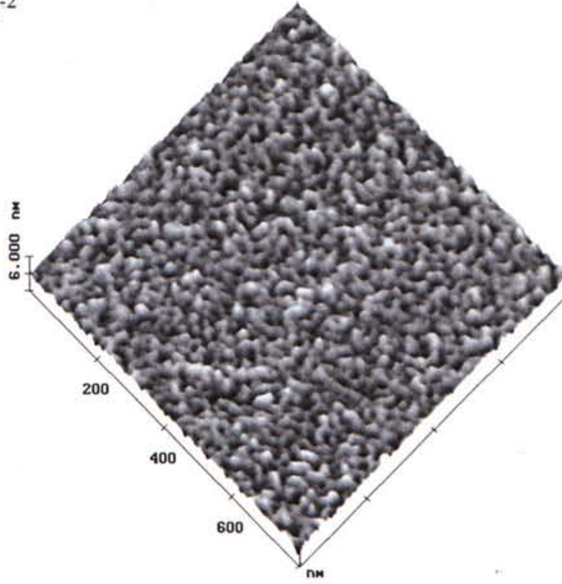

(b) 1×10^{16} ions cm^{-2}

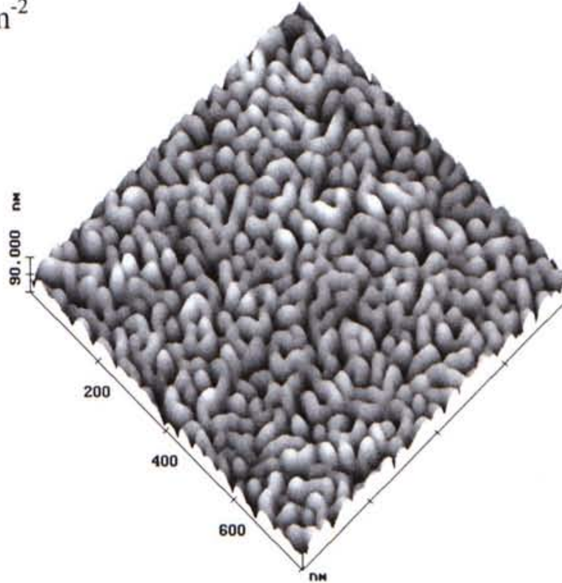

(c) 1×10^{17} ions cm^{-2}

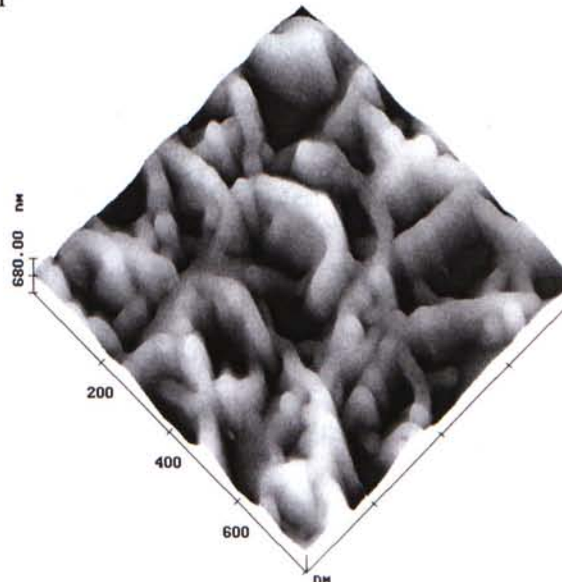

Table 4.2 Mean diameter and standard deviation of craters observed in various doses of Co-ion and self-ion implanted Ge

	Co-ion			self-ion		
dose / ions cm^{-2}	1×10^{15}	6×10^{15}	1×10^{16}	1×10^{15}	6×10^{15}	1×10^{16}
mean diameter / nm	14.86	22.59	26.91	16.35	24.35	29.19
standard deviation / nm	3.81	6.58	9.22	4.22	6.67	8.29

Complex porous structures are formed at a dose of 6×10^{16} and 1×10^{17} ions cm^{-2} (Fig. 4.1(d) and (e)). At higher dose, 6×10^{17} ions cm^{-2} (Fig. 4.1(f)), tall protrusions in irregular shape are seen. C-ion implanted Ge samples do not show any distinctive morphological features in the given doses. Small holes with increasing density are observed with increasing doses (Fig. 4.2). Figure 4.3 reveals self-ion implanted Ge samples showing a very similar trend and shape as that of Co-ion implanted Ge samples. The mean values of the crater diameters and their standard deviations at various doses are also given in Table 4.2. They are of comparable values with the Co-ion implanted ones.

Similar cellular structures (Fig. 4.1(c)) are seen from samples prepared by Chen using Co-ion implantation into Ge operating at an extraction voltage of 70kV [28,29]. Our AFM micrographs obtained for self-ion implanted Ge are in good agreement with that obtained by Professor Wilson [15] using high-resolution SEM under comparable conditions. To further confirm the micrographs obtained by AFM, high-resolution SEM (JOEL 6300F) micrographs, with the help of Dr. M. L. Yu from HKUST, are observed on the samples prepared on a similar condition as our samples.

They are shown in Fig. 4.4. From the plan view of Fig. 4.4(a), porous structure is seen on the surface of the Ge sample. The mean diameter of the craters is 24.75nm with a standard deviation of 9.50nm. The magnitude is comparable to that obtained from the AFM micrographs given in Table 4.2.

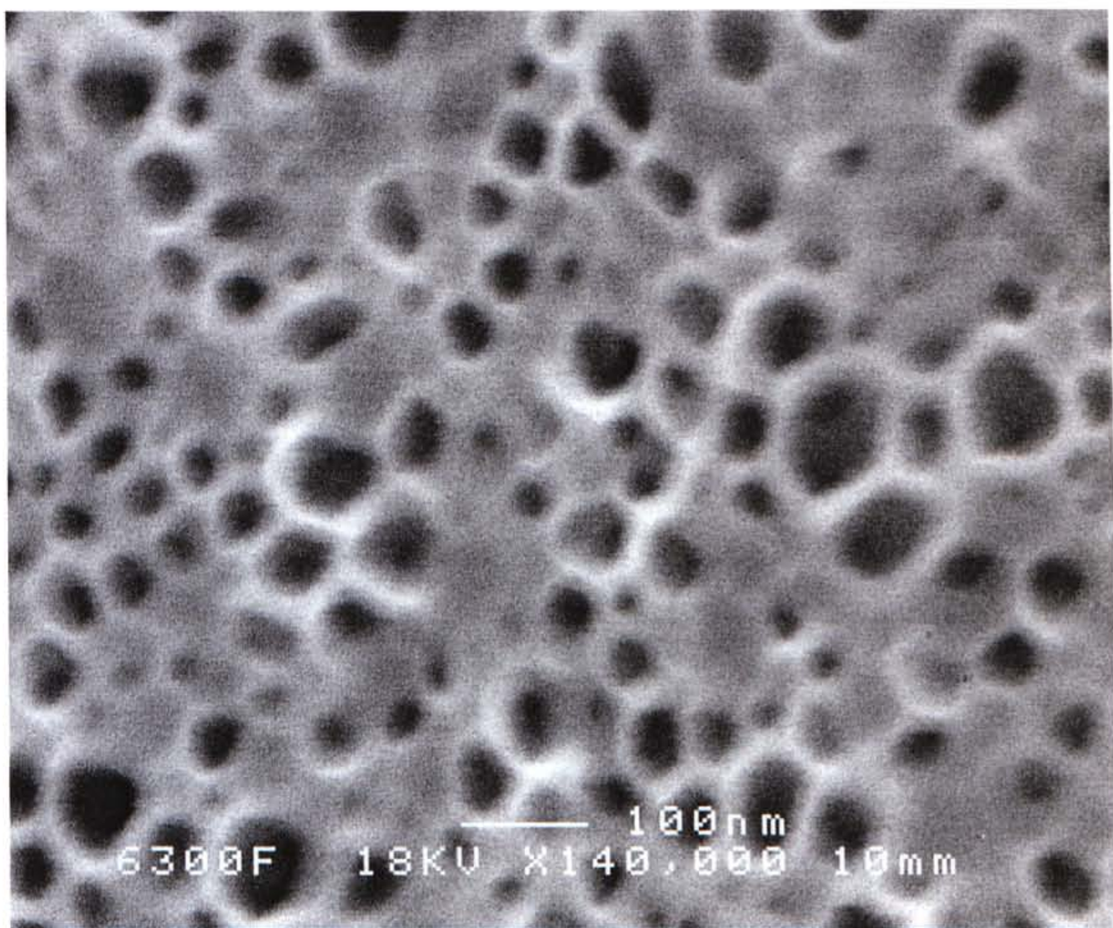

Fig. 4.4(a) Plan view high-resolution SEM micrograph of Co-ion implanted Ge(111) at a dose of 5×10^{16} ions cm^{-2}, mean current density of 15 $\mu A\ cm^{-2}$ and an extraction voltage of 70kV

A cross-section high-resolution SEM micrograph of the same sample is shown in Fig. 4.4(b) showing a honeycombed structure extending to a depth around 304nm.

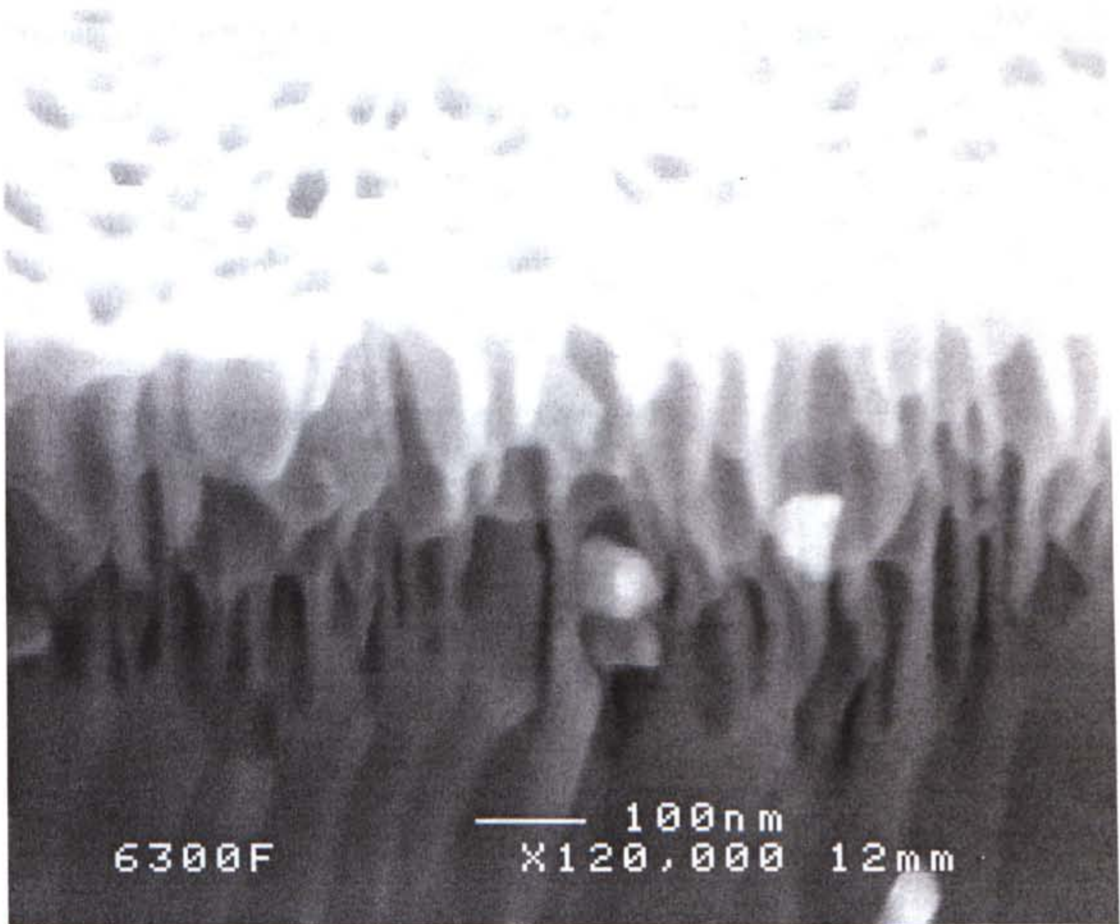

Fig. 4.4(b) Cross-section high-resolution SEM micrograph of Co-ion implanted Ge(111) at a dose of 5×10^{16} ions cm^{-2}, mean current density of 15 $\mu A\ cm^{-2}$ and an extraction voltage of 70kV

The boundary between the bombarded and unbombarded area is shown below in Fig. 4.5. The topography is typical of that observed for specimens where the mean current density is 15 μA cm^{-2}, and below a dose of 10^{17} ions cm^{-2}. The density and diameter of the craters are observed to decrease gradually across the boundary from the bombarded side. It is as expected because of the imperfect collimation of the incident beam, and bombardments made by the sputtered or reflected particles. The boundary will not be clearly cut. However, because of the slope correction made to compensate for tilt of the sample relative to the scanning plane and the bowing of the piezo tube in using AFM, it is difficult to tell whether the bombarded area is in a higher or lower level than the unbombarded one.

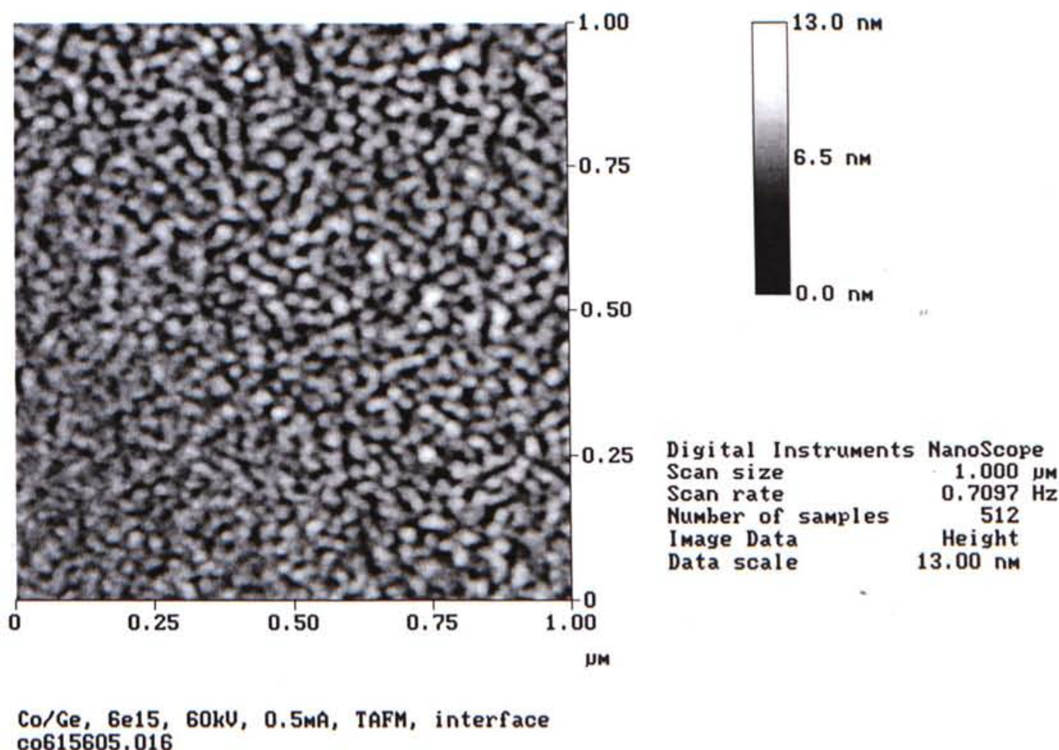

Fig. 4.5 Tapping mode AFM micrograph of Ge surface at the boundary between the bombarded and unbombarded areas. Bombarded by Co-ion at a dose of 6×10^{15} ions cm^{-2}, mean current density of 15 μA cm^{-2} and an extraction voltage of 60kV

While the horizontal dimensions of the surface features are described by the mean crater diameter and standard deviation, the variation in vertical dimensions are indicated by the surface roughness. The root mean square (RMS) roughness is defined by

$$R_{rms} = \left\{ \frac{\left[\sum_{n=1}^{N} \left(Z_n - \overline{Z} \right)^2 \right]}{N-1} \right\}^{1/2} \tag{4.1}$$

where Z_n is the height measurement of pixel n (from a total of N pixels, and N=256 × 256 throughout the whole experiment), and $\overline{Z}$ is the arithmetical mean height. The RMS roughness against dose of different samples is plotted below in Fig. 4.6.

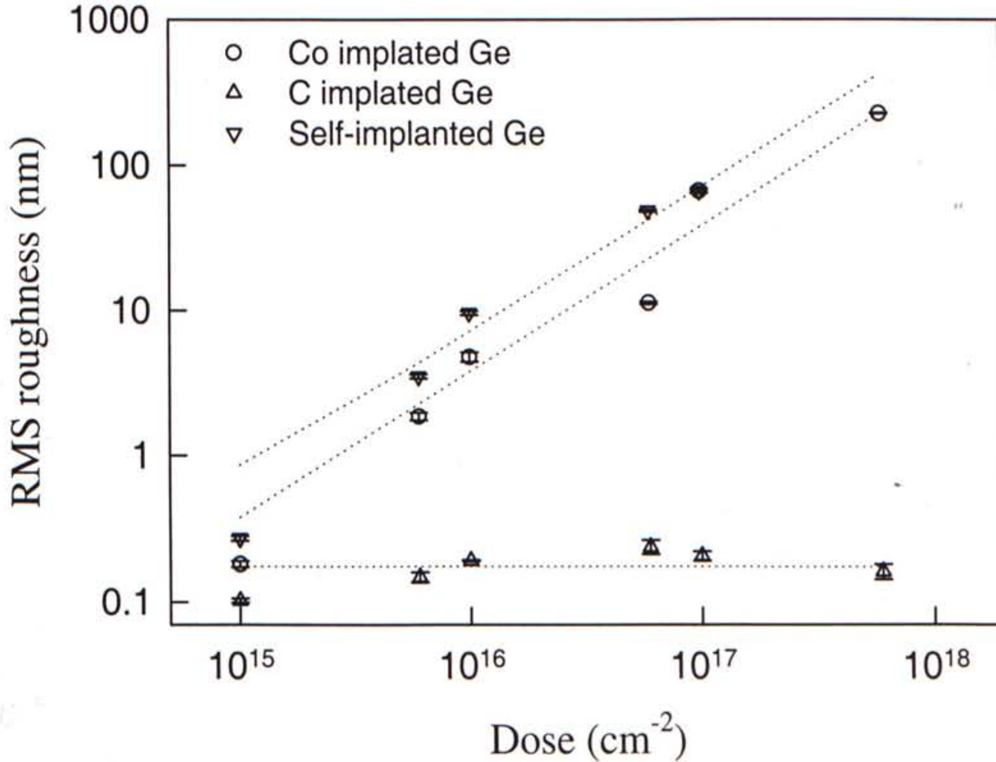

Fig. 4.6 RMS roughness vs dose of different samples. Dotted lines are exponentially fitted curves as a guide to the eyes

The RMS roughness of virgin Ge sample is < 0.1 nm. One can notice that the larger the mass of the projectiles, the larger the RMS roughness of the bombarded samples.

As revealed from the AFM micrographs of Co-implanted and C-implanted samples (Fig. 4.1 and Fig. 4.2), the surface morphology of the bombarded samples depends very much on the mass of the projectiles. However, potential phase formation between the projectile and target atoms seems not playing an important role as no appreciable difference is seen on the AFM micrographs between Co-implanted and self-implanted samples (Fig. 4.1 and Fig. 4.3). This is as expected because the implantation temperature is relatively low, less than 140°C (from Table 4.1), when compared with the activation energy of the corresponding phase transformation. By conventional XRD measurement, no new phase had been formed in Co-implanted and C-implanted samples, except at very high dose (6×10^{17} ions cm^{-2}) of Co-implanted one. It will be discussed in more details in the next chapter when high beam current density is considered.

It is suggested by Professor Wilson [20] that in low dose implantation, $\sim10^{11}$ ions cm^{-2}, when the number of craters is seen to have a 1:1 correlation with the number of ion impacts, craters formation is due to imbalance point-defect distribution in the cascade. When a projectile enters into a surface, it creates vacancies along the trajectory, and interstitials around the vacancies (Fig. 4.7). As a result, the centre of the cascade is rich in vacancies and the periphery is rich in interstitials.

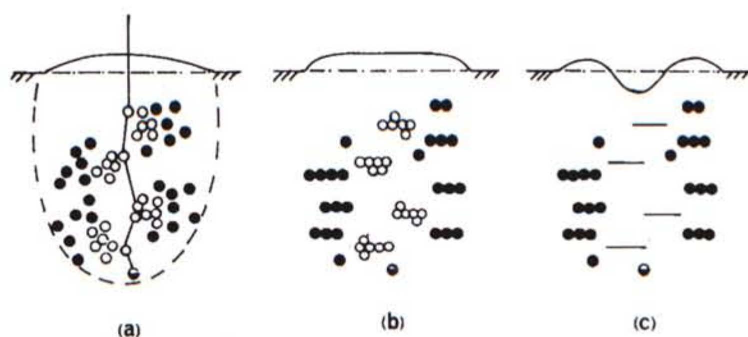

Fig. 4.7 Schematic illustration showing a) creation of vacancies and interstitials, b) formation of vacancy clusters and interstitial planes, c) collapse of the surface to fill in the vacancies forming a crater and raising of the periphery due to extra planes. o, vacancy; •, interstitials (After Wilson [20])

When the atoms rearrange themselves following the cascade, vacancy clusters will collapse to form dislocation loops and interstitials will condense as extra planes. Stress from these processes result in the sinking and raising of the surface and a crater is formed. Others suggested a slightly different mechanism. When the energy deposited by the projectile is high enough, a thermal spike will be induced leading to a localised pressure exceeding the elastic limit of the solid. The material yields plastically leaving a void.

When dose increases, morphology seen on the surface is caused by the intersection of individual craters by the surface. As discussed in the section of Background Theory, at least four phenomena [15] will further contribute to the evolution of the cell structure: variation of the sputtering yield with the angle of incidence, radiation damage swelling, enhancement of incident ion flux by reflection from steep slopes, and redeposition of sputtered atoms on cell walls. However, Appleton et al. [31] have shown that a free surface is not necessary for eruption of the amorphous phase to form craters or large columnar voids. The craters are not

initiated or amplified by a surface sputtering process. The rapid growth of voids into large holes is suggested to due to plastic flow.

At this stage, it is impossible to discuss the formation mechanism in a theoretical model. But still, we can have a closer look into the followings:

1. Can the surface morphology be created by the coalescence of smaller craters during medium dose ($10^{15} - 10^{16}$ ion cm^{-2}) implantation?
2. How important is the thermal spike playing a role in the crater formation?

Referring back to the section of Background Theory, the average number of displaced atoms in a cascade produced by a primary knock-on atom (PKA) of energy E, given by the modified Kinchin-Pease displacement damage function:

$$\langle N_d(E) \rangle = \begin{cases} 0 & (\text{for } 0 < E < E_d) \\ 1 & (\text{for } E_d \le E \le 2E_d/\xi) \\ \dfrac{\xi \nu(E)}{2E_d} & (\text{for } 2E_d/\xi \le E < \infty) \end{cases} \tag{2.12}$$

where $\nu(E)$ is the damage energy, that is the amount of energy lost to nuclear excitation, E_d is the displacement energy, and both analytical theory and computer simulation suggest a value ξ near 0.8.

To convert the above equation from the displaced target atoms produced by a PKA to that produced by a projectile, we make the following simplifications:

1. Neglect the energy loss in electronic stopping of the projectile before it collides with the target atom to produce a PKA. Therefore the energy of the projectile just before collision is still equal to the incident energy, E_o.
2. Assume there is only one collision between the projectile and the target atom. It means that only one PKA is produced throughout the life of the projectile.

Therefore we approximate the average number of displaced atoms produced by a projectile:

$$\left\langle N_d^{'}(E_o)\right\rangle = \frac{\xi\nu((1-K)E_o)}{2E_d} \qquad (4.2)$$

where K is the kinetic factor of the projectile. Another rigorous treatment is given in the book written by Michael Nastasi [4]. The damage energy, ν(E), is the energy that loses in nuclear collisions only. As a projectile loses energy in both electronic and nuclear collisions as it slows down inside the target. Only the latter process creates lattice disorder around the ion track and is responsible for radiation damage effects. Therefore, in considering the disorder created by the projectile, one must first determine the partition of energy between electronic and nuclear process. Averback *et al.* derived an expression for the ion damage energy using an integrodifferential equation. An approximation of the damage energy in reduced energy notation can be given as

$$\nu(\varepsilon) \cong 0.8\varepsilon \qquad (\text{for } \varepsilon < 1 \text{ and } Z_{\text{projectile}} > 5) \qquad (4.3)$$

where ε is the reduced energy given by

$$\varepsilon = \frac{M_2}{M_1 + M_2}\frac{a_{TF}}{Z_1 Z_2 e^2}E \qquad (4.4)$$

$$a_{TF} = \frac{0.8853a_o}{(Z_1^{2/3} + Z_2^{2/3})^{1/2}} \qquad (4.5)$$

M_1, M_2, and Z_1, Z_2 are the mass numbers and atomic numbers of the projectile and target respectively. a_{TF} is the Thomas-Fermi screening length and a_o is the Bohr radius (0.053 nm). Taking E_d to be 15 eV, the minimum displacement energy for Ge [32], and ξ=0.8, we can calculate the damage energy for each projectile by Eq. (4.3)-(4.5), and then the average number of displaced atoms by Eq. (4.2). The number of

displaced atoms for each projectile is also calculated by the Monte Carlo simulation for comparison. They are given below in Table 4.3.

One can see that the Monte Carlo simulation fits quite well with the calculated one in the Ge-ions and Co^{3+} ions. In general, the calculated values underestimate the average number of displayed atoms as we assume the nuclear collision takes place only once in the life of the projectile. Taking the density of Ge single-crystal to approximate the density of solid after implantation, and approximating the cascade volume by a sphere, we can calculate the mean diameter of the craters. They are shown in Table 4.4. The mean diameter measured from AFM micrographs are also copied from Table 4.2 and put aside for comparison.

Table 4.3 Average number of displaced atoms produced by the projectile using modified Kinchin-Pease displacement damage function and Monte Carlo Simulation

	Calculated		Monte Carlo Simulation			
	$\nu((1-K)E_o)$ / keV	$\langle N'_d(E_o)\rangle$	Displaced atoms / ion	Projected range (R_p) / Å	Longitudinal straggling $\langle \Delta X^2\rangle^{1/2}$ / Å	Transverse straggling $\langle \Delta Y^2\rangle^{1/2}$ / Å
Co^{+}	40	1067	1487	336	168	151
Co^{2+}	73	1947	2747	618	290	264
Co^{3+}	101	2693	2968	908	405	384
C^{+}	10	267	411	1122	442	546
Ge^{+}	43	1147	1170	295	148	125
Ge^{2+}	80	2133	2196	539	254	217

Table 4.4 Comparison among the mean diameter of single cascade calculated by modified Kinchin-Pease displacement damage function and Monte Carlo Simulation, and also the mean diameter of the craters observed in AFM micrographs

	Calculated	Monte Carlo Simulation	Measured from AFM micrographs
	mean diameter of single cascade / Å	mean diameter of single cascade / Å	mean diameter / Å
Co^{+}	17.9	20.0	148.6 – 269.1
Co^{2+}	21.9	24.6	
Co^{3+}	24.4	25.2	
C^{+}	11.3	13.0	too small to be measured
Ge^{+}	18.4	18.5	163.5 – 291.9
Ge^{2+}	22.6	22.8	

One can see that the mean diameters observed in the AFM micrographs are in general one order of magnitude larger than that of the single cascade. Therefore, at least, it is not contradictory that the craters seen on medium dose implanted surface are created by the coalescence of smaller voids during the ion bombardment.

How important is the thermal spike in the crater formation? The mean energy density deposited per atom, θ_D, in a collision cascade is an important quantity when evaluating the potential consequences that spikes may have on the properties of a solid. It has been shown [33] that collision cascade theory appreciably underestimates the number of displaced atoms whenever θ_D is larger than a few

tenths of an eV per atom. Moreover, when θ_D exceeds the heat of fusion of the solid, melting of the cascade volume may result and is suggested to be a possible reason for the formation of the crater.

The mean energy density in an individual cascade of volume V_{cas}, formed by an energetic projectile of energy E, can be approximated by [4]:

$$\theta_D = \frac{0.32\nu(E)}{NV_{cas}} = \frac{0.32\nu(E)}{N\delta^3 V_T} \tag{4.6}$$

where ν(E) is the damage energy as defined in Eq. (4.3). Assuming that the distribution of the damage energy can be represented by a Gaussian distribution, the amount of damage energy in one dimension, which will reside within ±1 standard deviation of the mean will be 68.27% of the total distribution. Thus, taking into account all three dimensions, the fraction of the damage energy residing within ±1 standard deviation of the mean will be $(0.6827)^3 = 0.32$. Therefore a factor of 0.32 is added to the damage energy. N is the atomic density of the target. To calculate the volume of individual cascade, we find the volume of the transport cascade, V_T, then correct it by multiplying the correction factor, δ^3. We approximate the volume by a sphere of the same volume. The radius of an equivalent sphere is given by

$$r = \left\langle \Delta X^2 \right\rangle^{1/6} \left\langle \Delta Y^2 \right\rangle^{1/3} \tag{4.7}$$

$$V_T = \frac{4\pi}{3}\left(\left\langle \Delta X^2 \right\rangle^{1/2} \left\langle \Delta Y^2 \right\rangle \right) \tag{4.8}$$

where $\langle \Delta X^2 \rangle^{1/2}$, $\langle \Delta Y^2 \rangle^{1/2}$ are the longitudinal straggling and transverse straggling obtained from Monte Carlo simulation. They are stated on Table 4.3 for reference. δ is found by looking up in the graph derived analytically by Sigmund *et al.* [4]: $\delta_{GE} \approx 0.6$, $\delta_{Co} \approx 0.5$, $\delta_C \approx 0.1$. Referring back to the section of Background Theory, Eq.

(2.15) can be used to calculate the corresponding temperature in absolute scale. The mean energy densities and temperature calculated are given in Table 4.5.

From Table 4.5, the mean deposited energy density is less than a few tenths of an eV per atom, so it eliminates the thermal spike contribution to the possibility of underestimate of the mean diameter in single cascade shown in Table 4.4. The corresponding temperatures in general do not exceed the heat of fusion of Ge. It, therefore, is reasonable to assume that the thermal spike effect is not playing an active role in crater formation in our experiment.

Table 4.5 Mean deposited energy density per atom and the corresponding temperature in degree Celsius

	mean deposited energy density, θ_D / eV	corresponding temperature / °C
Co^+	0.1444	844
Co^{2+}	0.0499	113
Co^{3+}	0.0428	58
C^+	0.1312	742
Ge^+	0.1488	878
Ge^{2+}	0.0535	141

4.3.2. RBS and ion channeling

Typical RBS and ion channeling spectra for the Co-ion implanted, C-ion implanted and self-ion implanted Germanium samples are given in Fig. 4.8 (a), (b) and (c) respectively.

Fig. 4.8 RBS random (R) and ion channeling (C) spectra for, (a) Co-implanted, (b) C-implanted, (c) self-implanted Ge samples at a dose of 1×10^{15}, 1×10^{17} cm^{-2}

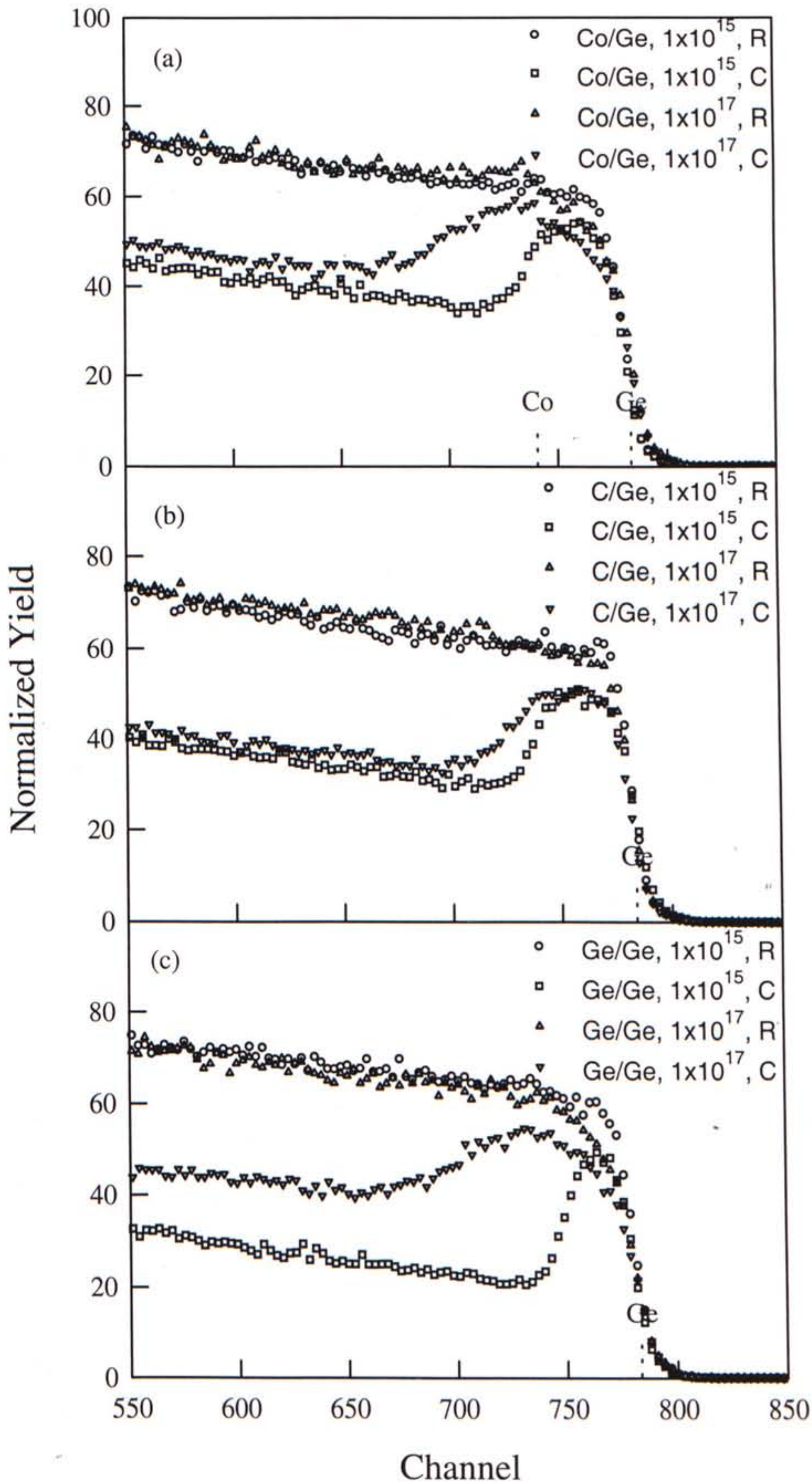

The depth of the damaged layer and the χ_{min} generally increase with increasing dose in all ions implanted samples. Depth of damaged layer is defined by the thickness counting from the surface up to the end of the back edge of the channeling yield. This is as expected, since higher dose will induce more damages, so decrease the crystallinity. Comparisons of depth of damaged layer and χ_{min} for various doses and implanted ions are shown in Fig. 4.9 and Fig. 4.10. C-ion implanted samples show a larger depth of damaged layer than that of Co-ion and self-ion implanted samples in medium dose, then becomes smaller in higher dose (around 6×10^{16} ions cm^{-2}). It is contradictory to the theoretical prediction as C-ion has a smaller mass and size, it should penetrate deeper into the target even in the higher dose cases. Deeper penetration is also obvious from the larger R_p of C-ion shown in Table 4.3. One possible explanation is that at higher dose, some of the implanted C-ions exist as substitutional impurities viewing in the <100> axis. The dissociation energy of the Ge-C bond is ~4.7 eV [34], compared to the ~2.8 eV required to break a Ge-Ge bond. This supports the formation of substitutional carbon in germanium. However, the Ge-C bond length in molecular compound is about 1.9 Å, much shorter than the 2.41 Å long Ge-Ge bond. This implies that the strain field around the substitutional carbon in germanium will be very large. A balance between the energy gained in forming Ge-C bonds and the increase in strain energy may make the formation of substitutional carbon defect unfavourable [34]. Another possible explanation is that because of the porous structure shown on the Co-ion and self-ion implanted surfaces (Fig. 4.1 and Fig. 4.3), projectiles have less chance to get bombarded, so can travel further. Therefore Co-ion and self-ion implanted samples have a deeper depth of damaged layer than it would otherwise be for a flat surface.

Fig. 4.9 Depth of damaged layer vs dose for the Germanium samples implanted by different ions

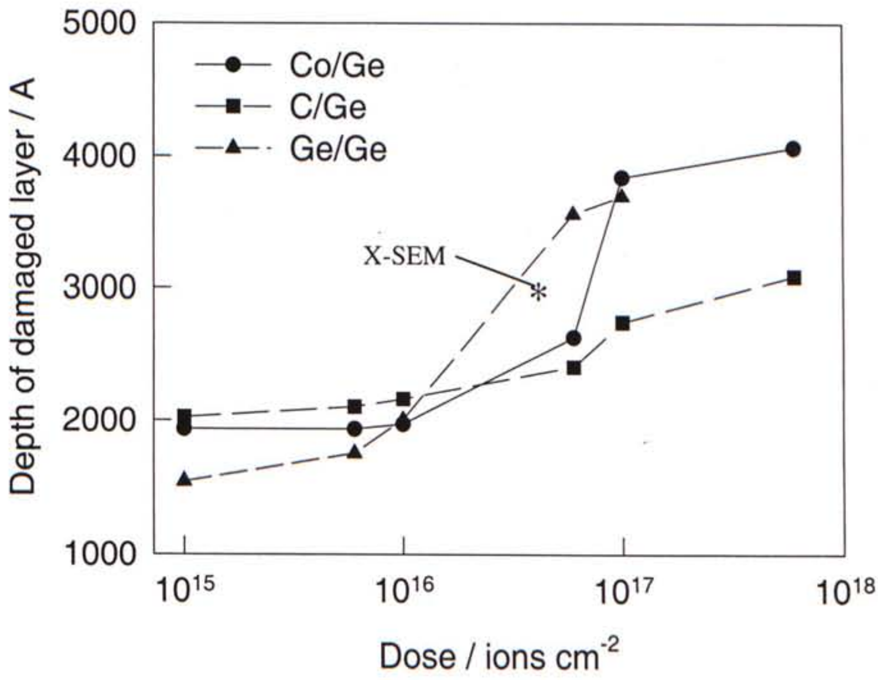

Fig. 4.10 χ_{min} vs dose for the Germanium samples implanted by different ions

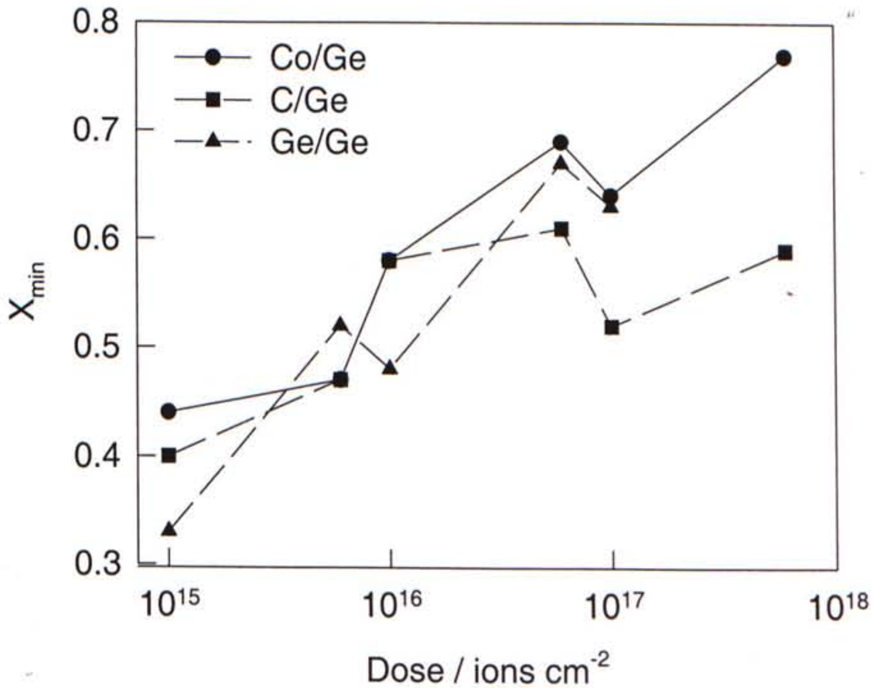

The depth of the honeycombed structure (Fig. 4.4(b)) observed by X-SEM is also indicated for reference in Fig. 4.9.

As the mass of germanium and cobalt ions are so close, it is theoretically impossible to separate their signals exactly from the RBS random spectrum. As a result, the concentration profile of the cobalt ions cannot be obtained exactly. Other techniques, such as XPS, have been employed, but the results have not yet been generated upon the completion of this thesis. The fitting of the random spectra starts from using the profile observed in Monte Carlo simulation. The software used is RUMP [35]. The concentration profile suggested from Monte Carlo simulation is shown in Fig. 4.11. The fitted spectrum is shown in Fig. 4.12. A dose of 1×10^{17} Co-ions cm^{-2} is taken as an example for spectrum fitting. As revealed in Fig. 4.12, more 'materials' present in the simulation than the random spectrum. This is not a problem that can be solved by adjusting the simulation profile. Because if the pump, where the simulation exceeds the random spectrum, is reduced by decreasing the cobalt concentration, the corresponding increase in germanium concentration will add it back.

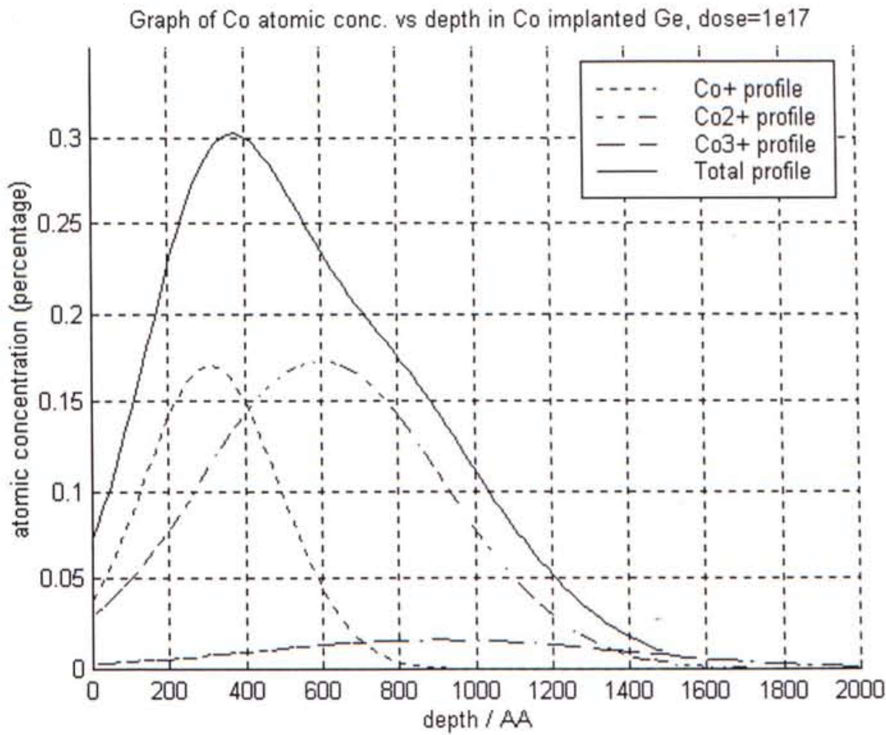

Fig. 4.11 Graph of Co-ion concentration profile calculated from Monte Carlo simulation. A dose of 1×10^{17} ions cm^{-2} is taken as an example

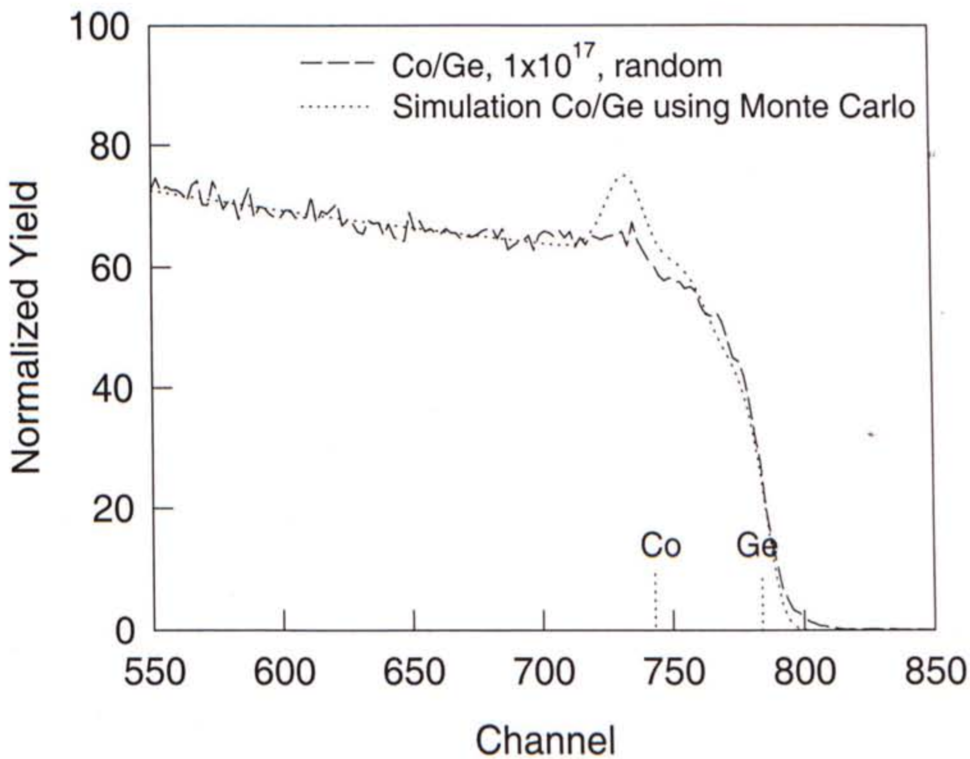

Fig. 4.12 Simulation of RBS random spectrum using the concentration profile obtained from Monte Carlo simulation

Therefore the only way to fit the random spectrum exactly is by introducing some impurities, such as carbon or oxygen, into the concentration profile to take up the space (Fig. 4.13). However, in this case, the concentration profile will be arbitrary, as the carbon and oxygen signals are too small to be distinguished when they overlap with the germanium substrate signals. Other techniques need to be employed to find out their concentrations. From Fig. 4.8(a) and (c), a surface yield deficit exists in the random spectra. It can be noticed from the rounding of the leading edge of the random spectra in the high dose samples. The surface yield deficit exists even in the self-ion implanted samples. No such surface yield deficit has been observed for the C-implanted samples. A throughout discussion of the origin of such yield deficit is presented in the next chapter.

Fig. 4.13 Simulation of RBS random spectrum using a concentration profile contained with carbon ions on the surface

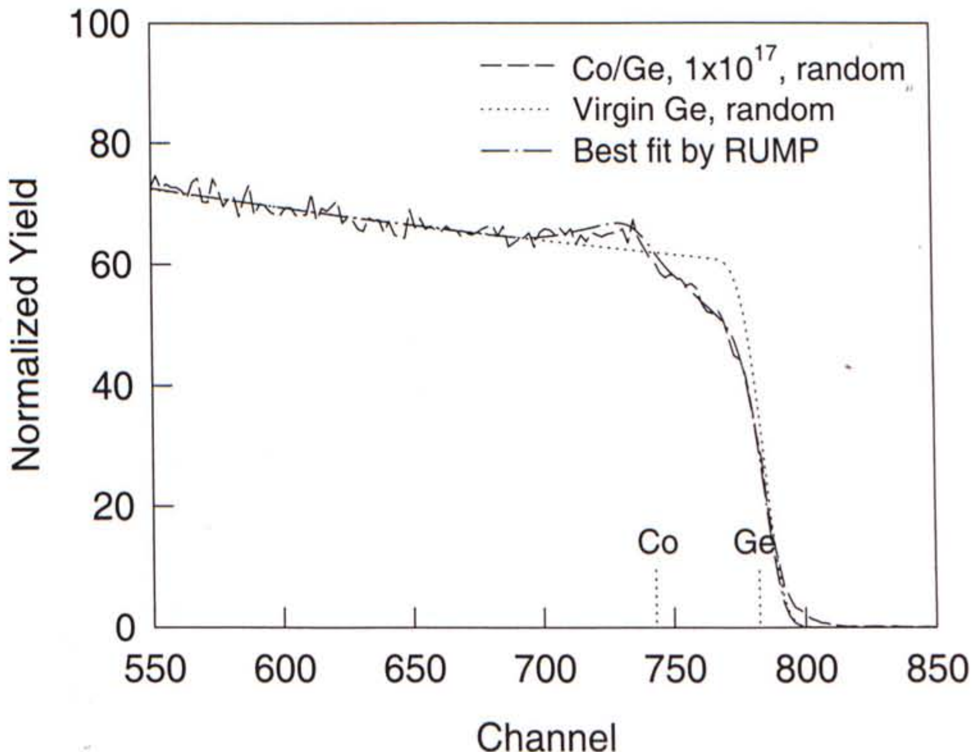

4.4. Conclusions

Cellular nanostructures were observed on both Co-implanted and self-implanted samples, but not in C-implanted ones. This is attributed to the much smaller mass and size of C-ions. Various mechanisms for crater formation are discussed, with special attention paying to whether the larger crater can be created by the coalescence of smaller craters in medium dose implantation ($10^{15} - 10^{16}$ ion cm^{-2}), and also the importance of the thermal spike effect in crater formation. By using Kinchin-Pease displacement damage function and Monte Carlo simulation, the mean diameter of a single cascade can be approximated to be around 11 - 25 Å, depending on the particular charge of ions. The mean crater diameter observed from AFM micrographs is an order of magnitude larger. Therefore, it is at least not contradictory to the suggested crater formation mechanism. The mean energy deposited per atom, θ_D, in a collision cascade is calculated to be around 0.05 – 0.15 eV, corresponding to a temperature around 60 - 880°C, which is still below the heat of fusion of Ge. Therefore the thermal spike effect may not be playing an active role in crater formation in our experiment. Ion channeling spectra for C-implanted samples show a smaller depth of damaged layer than the Co-implanted and self-implanted samples in higher dose implantation ($6\times10^{16} - 6\times10^{17}$ ion cm^{-2}). It is suggested that because of the porous complex structure shown on the Co-implanted and self-implanted surfaces, projectiles get less chance to be bombarded, thus results in a deeper depth of damaged layer than it would be for a flat surface. A surface yield deficit exists in the random spectra of Co-implanted, and self-implanted samples which make it impossible to fit the spectra without introducing impurities into the near surface

region. A more throughout discussion about the origin of surface yield deficit will be given in the next chapter.

CHAPTER 5

ION BEAM SYNTHESISED COBALT GERMANIDE ALLOY BY METAL VAPOUR VACUUM ARC IMPLANTATION

5.1. Introduction

Because of the increasing packing density and speed in the very large-scale integrated circuits (VLSI), reducing the interconnection resistance has long been an important issue. Metal silicides such as titanium disilicide ($TiSi_2$) and cobalt disilicide ($CoSi_2$) have been studied extensively for this purpose due to their low resistivity and good thermal stability [36-38].

In the last few years, $Si_{1-x}Ge_x$ alloy system has enjoyed a widespread interest and proved to be useful in optoelectronics, high-speed switching applications and other band gap engineered devices [39-40]. Many of these device structures require a metal-$Si_{1-x}Ge_x$ Ohmic contact with low resistivity. Titanium germanide ($TiGe_2$) and cobalt germanide ($CoGe_2$) have been shown to have a resistivity comparable to those of the corresponding silicides [41-42]. The formation of cobalt germanide by chemical vapor deposition, Co evaporation and rapid thermal annealing has been reported [42].

With the development of the metal vapor vacuum arc (MEVVA) ion source implanter, invented by Brown *et al.* [43], metal ions with high current density can readily be extracted. In this chapter, we report the formation of cobalt germanide by direct Co-ion implantation into single crystal Ge(100).

5.2. Experiments

The wafers used were chemomechanically polished n-type Ge(100) with less than 0.4 Ω cm resistivity. The substrate temperature is monitored by a thermocouple. The implantation was carried out in a JYZ-8010W MEVVA ion source implanter in normal incidence with an extraction voltage of 60kV, ion doses ranging from 6×10^{14} to 6×10^{18} ions cm^{-2}. The implanter was operated in pulse mode with mean current density being either 15 or 210 μA cm^{-2}. Because of the multiple charges nature of MEVVA, the particle flux corresponded to 34% Co^{+}, 59% Co^{2+} and 7% Co^{3+} [30]. The maximum temperature and the implantation time for each sample are shown in Table 5.1. XRD measurements were conducted by a SIEMENS D5005 X-Ray Diffractometer with a Cu Kα (1.540560Å) source in a θ-2θ configuration. AFM observations were made in air at room temperature using Digital Instruments Nanoscope III, operating in the tapping mode. Offline image processing of first order flattening and third order planefit were performed throughout. RBS random spectra with samples tilted at 7° and ion channeling spectra were obtained by HV Tandetron Accelerator at a 170° scattering angle with 2.0 MeV $^{4}He^{2+}$ particles.

5.3. Results and Discussion

5.3.1. XRD

In the low mean current density (15 μA cm^{-2}) samples, no germanide can be observed, until the dose comes up to 6×10^{17} ions cm^{-2} where Co_3Ge_2 [44] was formed. The XRD spectra of three samples implanted by a high mean current density (210 μA cm^{-2}) are shown in Fig 5.1.

Table 5.1 Summary of temperature, implantation time and XRD results of the Co as-implanted Ge samples

mean current density	Dose / cm^{-2}	Temp /°C	Implant. Time/min	XRD results		
				Co_3Ge_2	Co_5Ge_7	$CoGe_2$
15 μAcm^{-2}	6×10^{14}	36	<1			
	1×10^{15}	53	<1			
	6×10^{15}	53	1			
	1×10^{16}	60	2			
	6×10^{16}	98	13			
	1×10^{17}	105	38			
	6×10^{17}	110	289	✓		
210 μAcm^{-2}	6×10^{15}	93	<1	✓	✓	
	1×10^{16}	107	<1	✓	✓	
	6×10^{16}	150	3	✓	✓	
	1×10^{17}	258	18	✓		✓
	6×10^{17}	360	30	✓		✓
	1×10^{18}	430	46	✓	✓	✓
	6×10^{18}	509	343	✓	✓	✓

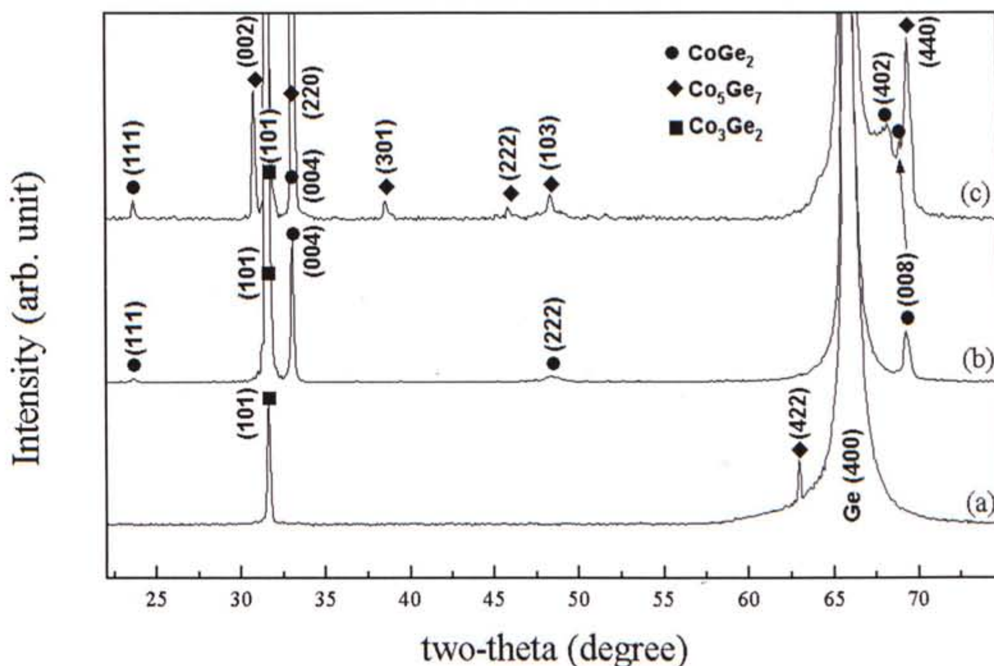

Fig. 5.1 XRD spectra of Co implanted Ge at a condition of (a) 6×10^{16} ions cm^{-2}, 210 μAcm^{-2} (b) 6×10^{17} ions cm^{-2}, 210 μAcm^{-2} (c) 6×10^{18} ions cm^{-2}, 210 μAcm^{-2}

Starting from a dose of 6×10^{15} ions cm^{-2} and up to 6×10^{16} ions cm^{-2} (Fig. 5.1(a)) both Co_3Ge_2 and Co_5Ge_7 were formed. By increasing the dose, $CoGe_2$ started to form. As can be seen in Fig. 5.1(b), at a dose of 6×10^{17} ions cm^{-2}, no Co_5Ge_7 is observed, Co_3Ge_2 still exists. More diffraction peaks of $CoGe_2$ are seen in the higher dose than the lower one signaling a better crystallinity. When the dose was up to 1×10^{18} ions cm^{-2}, Co_5Ge_7 reformed and more diffraction peaks of Co_5Ge_7 can be observed at a dose of 6×10^{18} ions cm^{-2} (Fig. 5.1(c)). A summary of the XRD results is given in Table 5.1. Therefore the sequence of phase formation of cobalt germanides is:

$$Co_3Ge_2 \rightarrow Co_3Ge_2, Co_5Ge_7 \rightarrow Co_3Ge_2, CoGe_2 \rightarrow Co_3Ge_2, CoGe_2, Co_5Ge_7 \quad (5.1)$$

The results are readily expected by considering the beam heating effect and the implantation time (Table 5.1) of each sample. Co_3Ge_2 was formed in samples of

6×10^{17} ions cm^{-2}, 15 μA cm^{-2} and 6×10^{15} ions cm^{-2}, 210 μA cm^{-2}. The dramatic differences in dose and implantation time indicate the temperature of the reaction to be the dominating factor for phase formation in the early stage. Co_5Ge_7 formed at 6×10^{15} ions cm^{-2}, 210 μA cm^{-2} and then transformed completely into $CoGe_2$ at 1×10^{17} ions cm^{-2} with temperature around 258°C. Co_5Ge_7 reformed at higher dose around 430°C. The temperatures of phase formation are comparable to that reported before ($CoGe_2$: 300°C, Co_5Ge_7: 425°C) [42] where the samples were made by Co evaporation and rapid thermal annealing.

The sequence of phase formation due to implantation has always been under debate [45]. From a solely thermodynamic point of view, the phase with the most negative heat of formation has the largest driving force and is therefore expected to form first. As the values of the heat of formation of Co-Ge compound are not available, we infer their relative values from the Co-Ge binary phase diagram according to Li. [46]. Referring to the phase diagram given by M. Hansen *et al.* [47] (Fig. 5.2), the heat of formation of Co-Ge compounds in ascending order (most negative on the left) is determined below:

$$Co_3Ge_2 \rightarrow Co_5Ge_7 \rightarrow CoGe_2 \quad (5.2)$$

Comparing sequences (5.1) and (5.2), the first phase formed and the order of formation of the other two phases match with that predicted by the thermodynamics. It is suggested that more than one phase form at one time because forming a mixture of these phases can lower the energy of such a non-equilibrium system. Co_5Ge_7 reformed at higher temperature because the thermodynamic factors no longer dominate the whole reaction process. Kinetic constraints have to be taken into consideration in the later stage.

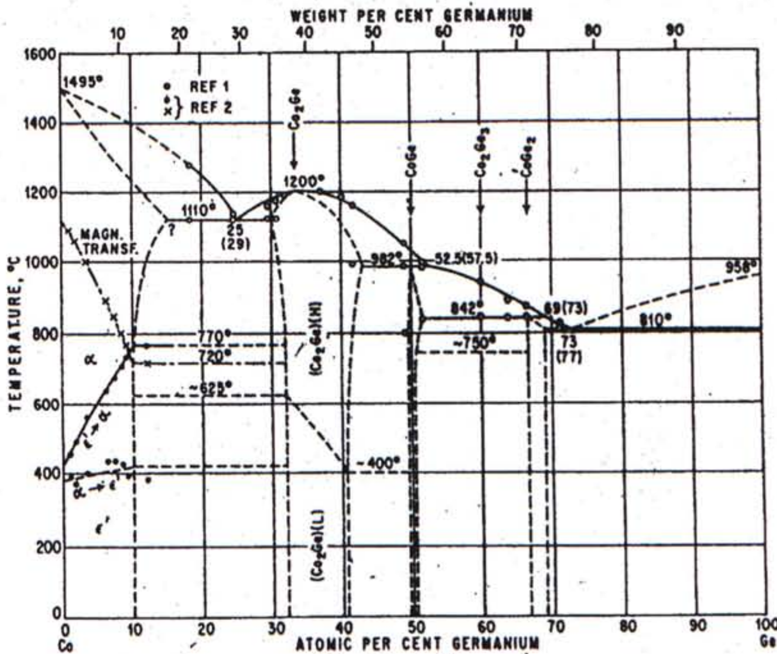

Fig. 5.2 Binary phase diagram of Co-Ge compound (After M. Hansen *et al.* [47])

5.3.2. *AFM*

As dimensions are being scaled down, it is of interest to gain some idea of the roughness introduced by implantation. Fig. 5.3 shows the tapping mode AFM micrographs of the low and high mean current density samples. Note that the scan area of Fig. 5.3(a) is 800nm × 800nm, while that of Fig. 5.3(b) is 5μm × 5μm in order to view the overall structure more clearly. For the low mean current density samples, cellular nanostructures are observed in the doses ranging from 6×10^{15} to 6×10^{16} ions cm^{-2}. At a dose of 1×10^{17} ions cm^{-2} (Fig. 5.3(b)), a complex porous structure is seen. The Digital software obtains the root mean square roughness (RMS roughness) of each sample. For each sample, the standard deviation of the RMS roughness of 4 micrographs is calculated and plotted as the error bar in Fig. 5.4. One can see the RMS roughness follows quite well with an exponential function.

Fig. 5.3 Tapping mode AFM micrographs of Co implanted Ge at a condition of
(a) 1×10^{16} ions cm^{-2}, 15 μA cm^{-2}, 800nm×800nm

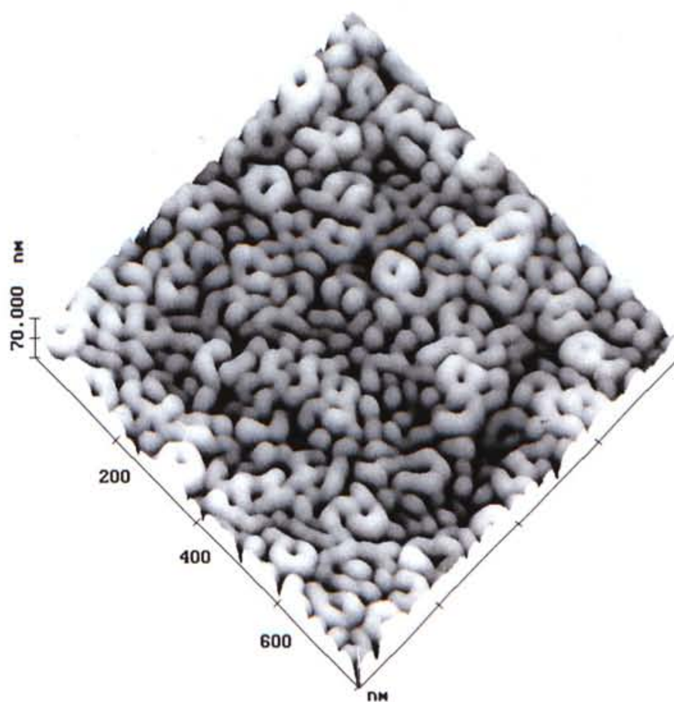

(b) 1×10^{17} ions cm^{-2}, 15 μA cm^{-2}, 5μm×5μm

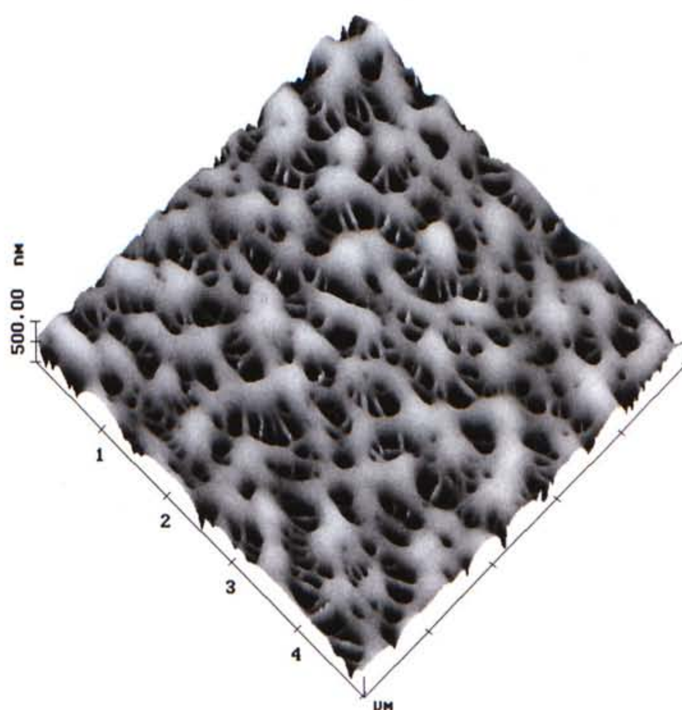

(c) 1×10^{16} ions cm^{-2}, 210 μA cm^{-2}, 1μm$\times$1μm

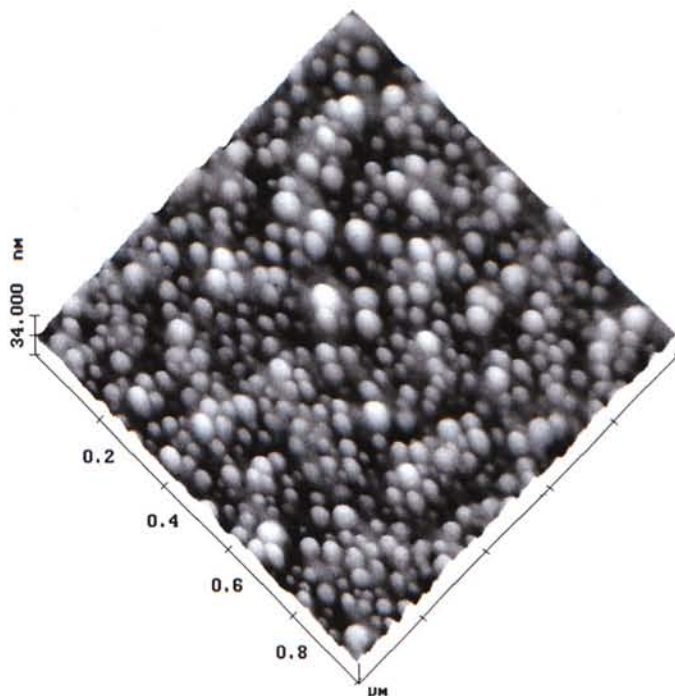

(d) 1×10^{17} ions cm^{-2}, 210 μA cm^{-2}, 1μm$\times$1μm

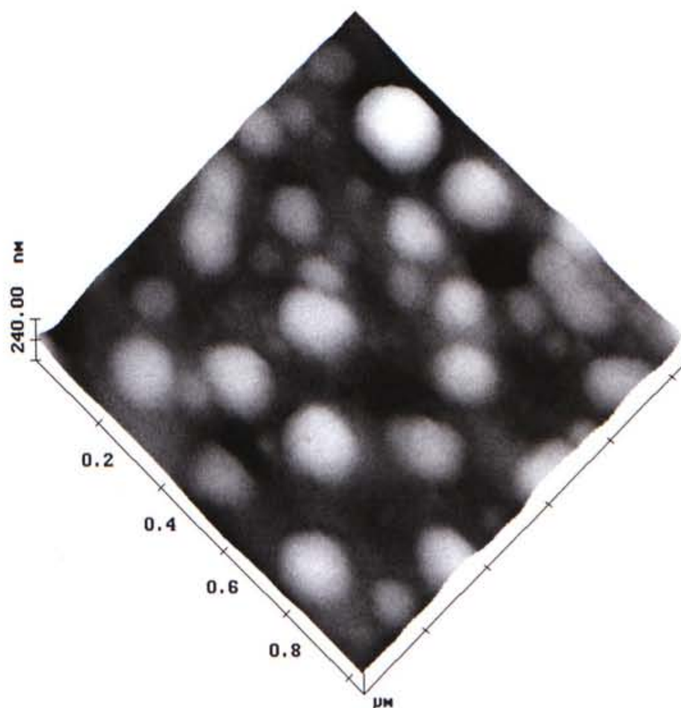

For the high mean current density samples, completely different morphologies are seen (Fig. 5.3(c) & 5.3(d)). Protrusions are formed on top of some secondary features. The RMS roughness goes down first with increasing dose, then goes up again, following quite well with a 3rd order polynomial (Fig. 5.4). At doses higher than 6×10^{16} cm^{-2}, the protrusions grew in diameter as well as in height. At 6×10^{17} cm^{-2}, the protrusions agglomerated and formed islands. We expect the morphological difference between low and high mean current density samples be mainly due to temperature. At high temperature, damage annealing, bulk and surface diffusion are greatly enhanced. Therefore, there is enough energy for agglomeration, columnar growth and island formation. Similar protrusions are also reported in metal-Si system [48].

Fig. 5.4 RMS roughness vs dose for the low and high mean current density samples

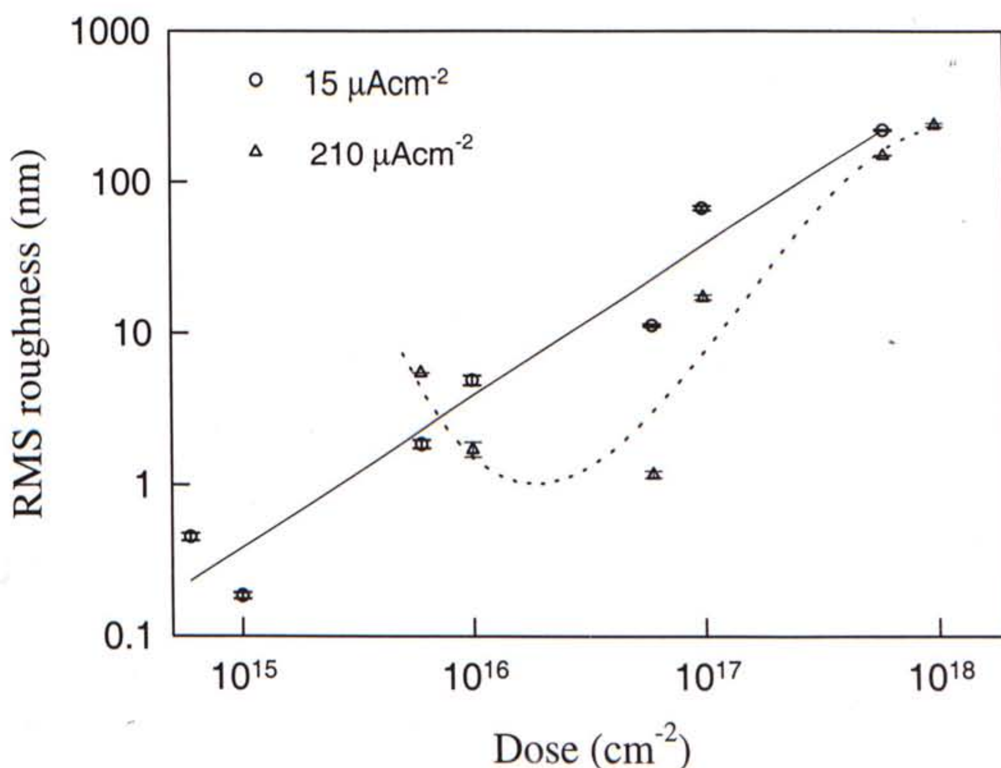

5.3.3. RBS and Ion channeling

Typical RBS and ion channeling spectra for the low and high mean current density samples are shown in Fig. 5.5(a) and 5.5(b), respectively.

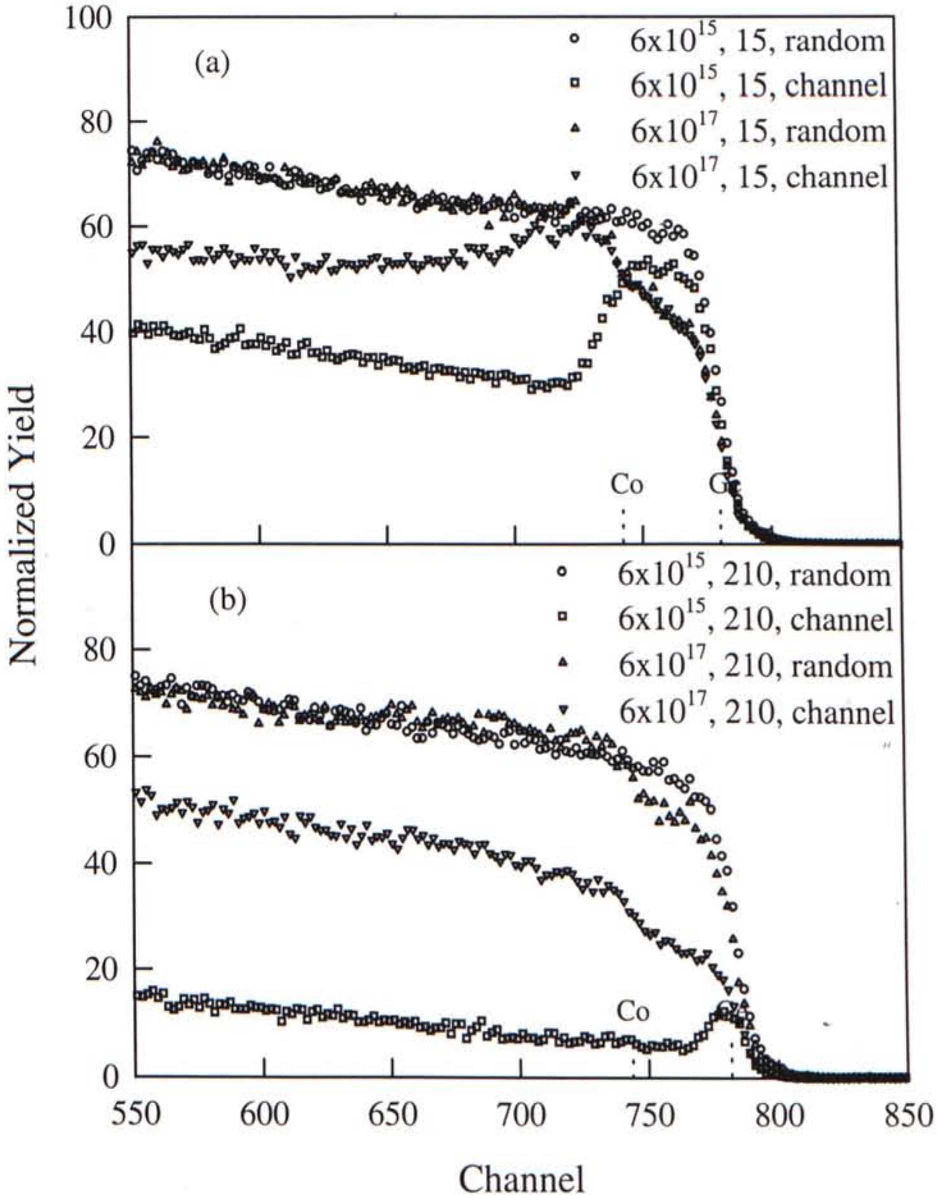

Fig. 5.5 RBS and ion channeling spectra of Co implanted Ge at a condition of (a) low mean current density, 6×10^{15} ions cm^{-2}, 6×10^{17} ions cm^{-2}, (b) high mean current density, 6×10^{15} ions cm^{-2}, 6×10^{17} ions cm^{-2}

As revealed in Fig. 5.5(a), in the low mean current density samples, for a dose up to 6×10^{15} ions cm^{-2}, the random spectra do not show much difference from a virgin crystal. Starting from 6×10^{16} ions cm^{-2}, a large yield deficit occurs in the near surface region of the random spectra when compared with the virgin one. For those random spectra with large yield deficit, when fitted by RUMP or DATAFURNACE [16], show smaller counts in the near surface region than the simulated one. An example is given in Chapter 4 (Fig. 4.12). The surface yield deficit may be due to:

(a) the stopping cross-section of the scattering particles with the presence of the implanted Co atoms does not follow strictly the Bragg rule, which is the assumption taken by the simulation software. Referring to previous XRD results, no Co-Ge compound was formed until a dose of 6×10^{17} ions cm^{-2}, 15 $\mu A\ cm^{-2}$. Therefore the changing of the stopping cross-section is merely due to the presence of Co atoms, but not Co-Ge compound. However, this may not be the full explanation as a similar yield deficit is seen in Ge self-ion implantation at 60kV, 1×10^{17} cm^{-2}, 15 μAcm^{-2} (Fig. 4.8(c)).

(b) contamination by impurities such as C and O due to the drastically increased surface area as suggested by O. W. Holland *et al.* [50]. We therefore carried out two non-Rutherford scattering experiments, including 3.04 MeV α-^{16}O and 1.76 MeV p-^{12}C. The determined concentrations of C and O in the near surface region are only comparable to the virgin one, so this reason may not apply in our data.

(c) decrease of density of Ge in the near surface region due to the dramatic cellular and porous structures as shown in the previous AFM micrographs. Moreover, the very rough surface will provide different energy-loss path for the particles even when they are scattered at the same depth from the surface. The effect of path

difference is the rounding of the leading edge of the random spectrum as the yields that originally count in one channel are now spread over the neighbours.

A concrete support for explanation (c) is to incorporate the decrease of Ge density into the simulation profile. To simplify our analysis, Ge self-implanted samples are used. This can avoid the uncertainty in separating the cobalt signals from the germanium signals in the case of Co-implanted samples. Fig. 5.6 as shown is the printout from AFM software. The sample is Ge self-ion implanted at 60kV, at a dose of 6×10^{16} ions cm^{-2}, and a mean current density of $15\mu Acm^{-2}$. The upper left corner gives the AFM picture. A very rough and porous surface can be seen. The middle shows the height distribution histogram. Zero depth means the highest point in the picture and is counted downwards. A nearly Gaussian distribution is observed. The graph on the right shows the integration of the histogram. It gives the area occupied by the sample material at a given depth. Using this information, a depth profile of germanium atomic fraction is constructed as below. The front part of the profile is cut as these data may be due to noise. The simulated spectrum with this profile fits very well with the experimental one (Fig. 5.7).

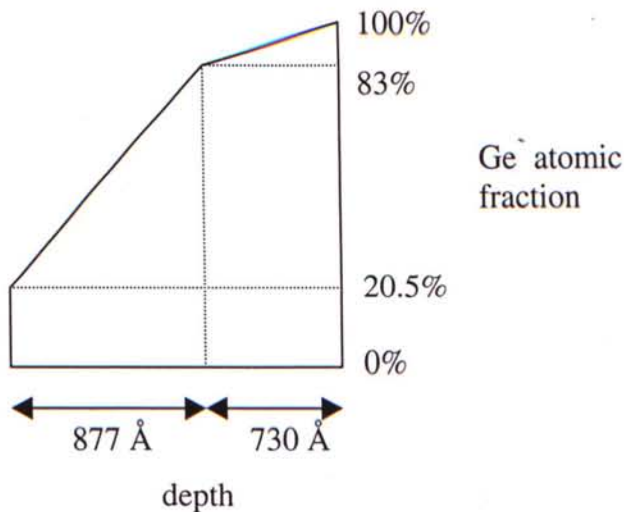

Fig. 5.6 Bearing analysis of self-implanted germanium sample, 6×10^{16} ions cm^{-2}, 15 $\mu A\ cm^{-2}$, by AFM software

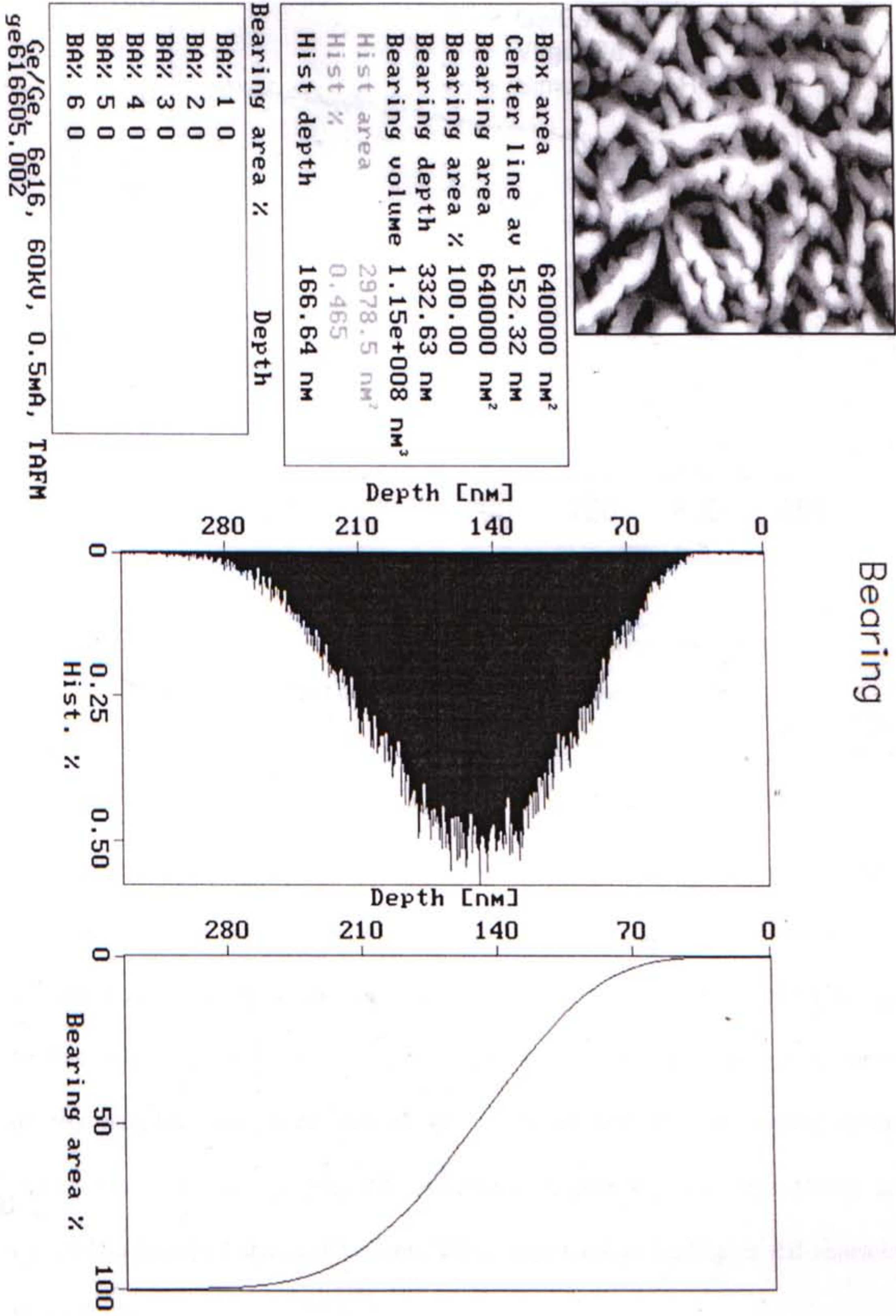

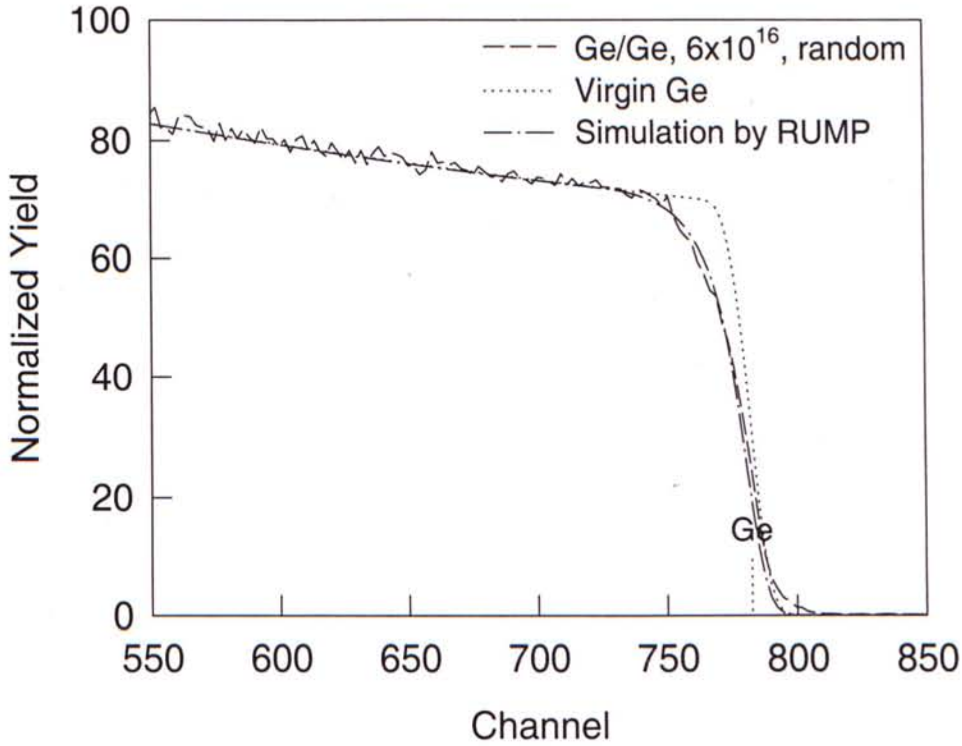

Fig. 5.7 Simulation of RBS random spectrum taking into account of the decrease of Ge density

The channeling spectra show that the thickness of the damaged layer (Fig. 5.8) increases with increasing dose. The thickness is counted from the surface up to the end of the back edge of the channeling yield. The thickness of the damaged layer applies only to the low mean current density samples. For the high mean current density samples, though the random spectra are similar, their channeling spectra show a much smaller χ_{min} (Fig. 5.8), indicating a higher degree of crystallinity, and no specific damaged layer can be seen. This is attributed to the higher self-annealing temperature.

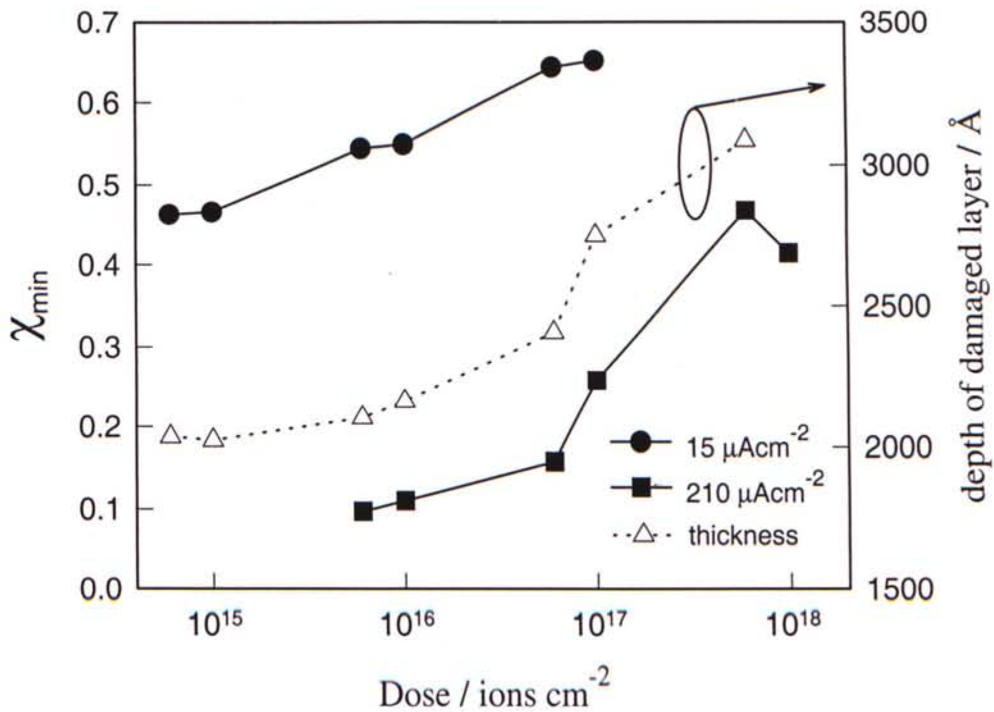

Fig. 5.8 χ_{min} of the low and high mean current density samples and the thickness of the damaged layer of the low mean current density samples

5.4. Conclusions

Cobalt germanides can be formed directly by high mean current density Co-ion implantation without postannealing. Because the high mean current density can readily produce the high temperatures required for the formation of various phases. MEVVA ion source implantation provides a possible manufacturing technique requiring only one single step. From XRD, Co_3Ge_2, Co_5Ge_7 and $CoGe_2$ were formed in the as-implanted samples. The first phase formed and the order of formation of various phases follow that predicted by thermodynamics, although more than one

phase may form in one time. Dramatic cellular and columnar nanostructures were observed in the low and high mean current density samples respectively. RBS reveals a yield deficit in the near surface region which may be attributed to the stopping cross-section not following strictly the Bragg rule, or the decrease of Ge density due to the cellular and porous structures. The coming studies aim at forming a layer consisting of $CoGe_2$ only so that the lowest resistivity can be utilized.

CHAPTER 6

TIP ARTIFACTS IN ATOMIC FORCE MICROSCOPE IMAGING OF ION BOMBARDED NANOSTRUCTURES ON GERMANIUM SURFACES

6.1. Introduction

The Atomic Force Microscope (AFM), developed in 1986 by Binning *et al.*, has become a widely used tool for investigating surfaces with high spatial resolution. Due to its large dynamical range, the AFM has been used to analyses surface and interfaces on various levels ranging from atomic resolution to more technological applications such as imaging nano-fabricated semiconductor structures.

However, one basic problem common to all scanning probe microscope techniques is the finite shape of the tip, which will convolute with the sample morphology to produce the image [51-53]. The amount of distortion depends on the relative size of the features on the sample surface and the tip. K. L. Westra *et al.* [54] suggested a criterion to judge whether the distortion of an AFM image is undetectable by eye in viewing a columnar thin film. The criterion is base on the ratio of radius of curvature of the sample surface feature and that of the tip. Others suggested ways to direct image the tip shape by AFM itself [55], and after obtaining the tip shape, how to deconvolute the real sample surface morphology [56].

In this chapter, we investigate the tip artifacts in the AFM images that we have presented in the previous chapters. Some of the material in this chapter is taken from a paper [57], in which the writer of this thesis is one of the authors.

6.2. Experiments

Chemomechanically polished n-type Ge(100) wafers with resistivity being less than 0.4 Ω-cm were used. The implantation was carried out in a JYZ-8010W MEVVA ion source implanter in normal incidence operating at an extraction voltage of 60kV, ion doses ranging from 6×10^{14} to 6×10^{17} ions cm^{-2}. The implanter was operated in pulse mode with mean current density being 15 μA cm^{-2}. Because of the multiple charges nature of MEVVA, the particle flux corresponded to 34% Co^{+}, 59% Co^{2+} and 7% Co^{3+} for Co-ion implantation [30].

The AFM observations were made in air at room temperature using Digital Instruments Nanoscope III, operating in both the contact mode and the tapping mode. A slope correction to compensate for tilt of the sample relative to the scanning plane was performed by offline fitting a first order polynomial to the image and then subtracted it from the image. The image was flattened further using a third order planefit to compensate for the bowing of the piezo tube.

6.3. Results and Discussion

Before tapping mode AFM has been used, contact mode AFM was being used to capture the surface morphology of the implanted germanium samples. However, severe distortion has been observed when compared with the literature and the SEM pictures (Fig. 4.4(a)). Contact mode AFM and tapping mode AFM micrographs of the same sample are shown in Fig. 6.1 (a) and (b), respectively. The granular structure shown on the contact mode AFM micrograph is due to the relative large size of the tip used when compared with the dimension on the surface features.

Fig. 6.1 (a) Contact mode AFM micrograph of Co-implanted Ge at a dose of 6×10^{16} ions cm^{-2}, 15μA cm^{-2}

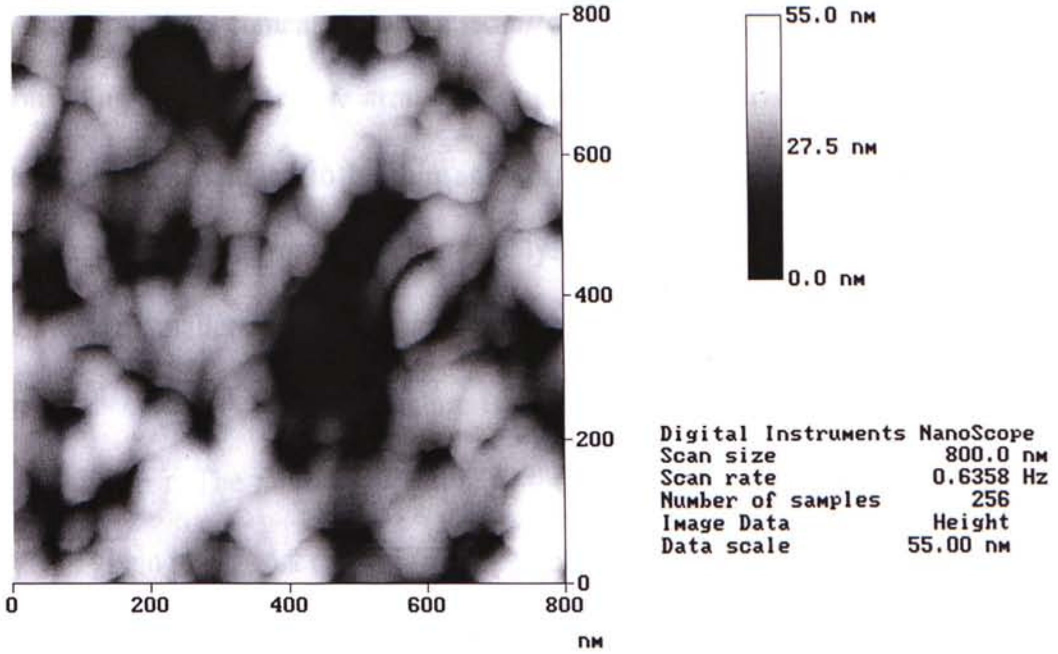

(b) Tapping mode AFM micrograph of Co-implanted Ge at a dose of 6×10^{16} ions cm^{-2}, 15μA cm^{-2}

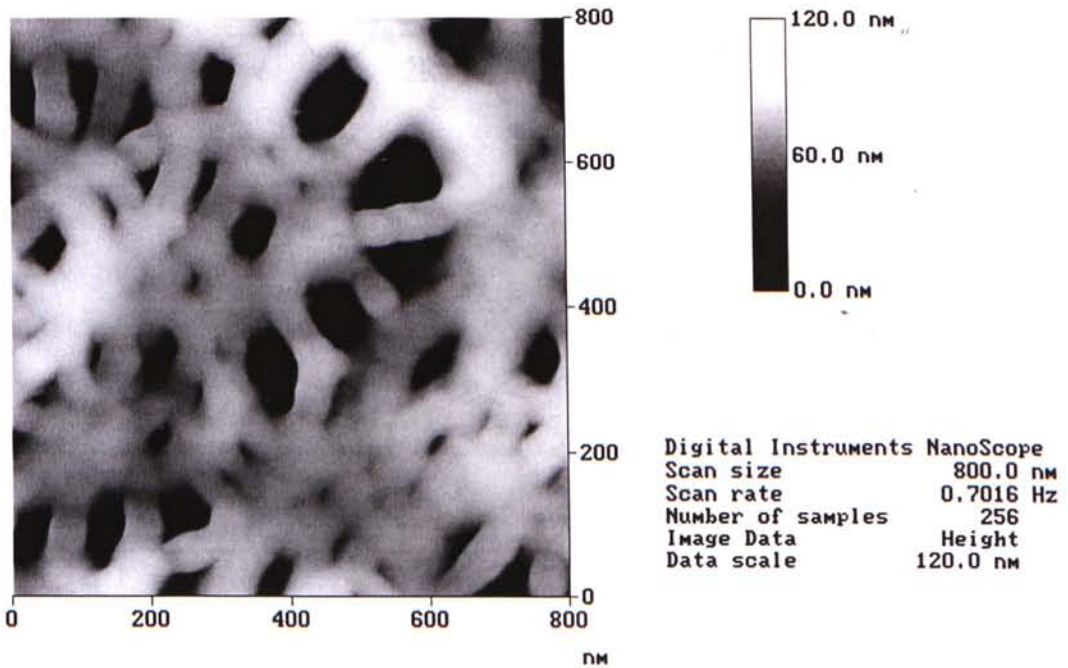

As suggested in the paper [57], a schematic is shown in Fig. 6.3 to explain the origin of tip artifacts presented in Fig. 6.1(b). For the sake of simplicity, we assume the AFM tip to be a conical tip with a radius of curvature, R, and the cellular surface as consisting of a consecutive array of circular craters. The radius of the crater is r. Crater walls are assumed to be thin and stiff, so that the interactions between the surface and tip depend on the geometry only. As shown in Fig. 6.3(a), when the tip size is much smaller than the crater size, R<<r, the tip tracks the surface features relatively accurate. A cellular structure is revealed in the AFM micrograph having a crater radius ≈ r. The radii of curvature of the tip used in contact mode and tapping mode are given in Fig. 6.2 (a) and (b) respectively.

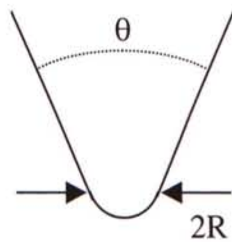

(a) Si_3N_4 tip

- $R = 35 \pm 15$ nm
- $\theta \geq 45°$

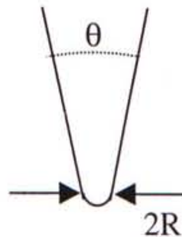

(b) Si tip

- $R = 15 \pm 5$ nm
- $\theta \leq 30°$

Fig. 6.2 Tip details in (a) contact mode AFM, (b) tapping mode AFM

Conversely, if the tip size is comparable or larger than the crater size, R>r, the AFM micrograph is not a representative of the real surface features. It is because the point where the tip and the surface are in contact is not necessarily the apex or area near apex of the tip. The crater radius observed from the tapping mode AFM as shown in Table 4.2 ranges from 7.5nm – 13.5nm, from a dose of 1×10^{15} to 1×10^{16} ions cm^{-2}. The measured values are comparable to the tip radius. Therefore the actual crater radius may be even larger than we have observed in the AFM micrographs. However, the image distortion is minor as it is the measured values that are close to the tip radius, not the real values. Moreover, the measured values are in good agreement with that obtained from high resolution SEM (Fig. 4.4(a)), 12.4nm, for a dose of 5×10^{16} ions cm^{-2}. For higher dose, the dimension of surface features is around a few tens to hundreds of nanometer, so the distortion is further less.

Deconvolution of the real surface morphology generally is a difficult task and is done through computer simulation. One very simple way to gain an idea of the lateral extension of the real surface morphology is to invert the AFM micrographs. As shown in Fig. 6. 3(b), the radius of the craters in the inverted image will still preserve the original radius r, with a phase shift of r. Though the vertical height information may not be available. An inverted image of Fig. 6.1(a) is shown in Fig. 6.4. The mean crater radius obtained from the inverted image is 64.87 nm with a standard deviation of 14.19 nm, a bit bigger than that obtained from the tapping mode AFM micrograph (Fig. 6.1(b)), which has a mean crater radius of 55.36 nm with a standard deviation of 22.61 nm.

Fig. 6.3 Schematic of AFM imaging of large and small crater when compared with tip radius

(a) R<<r

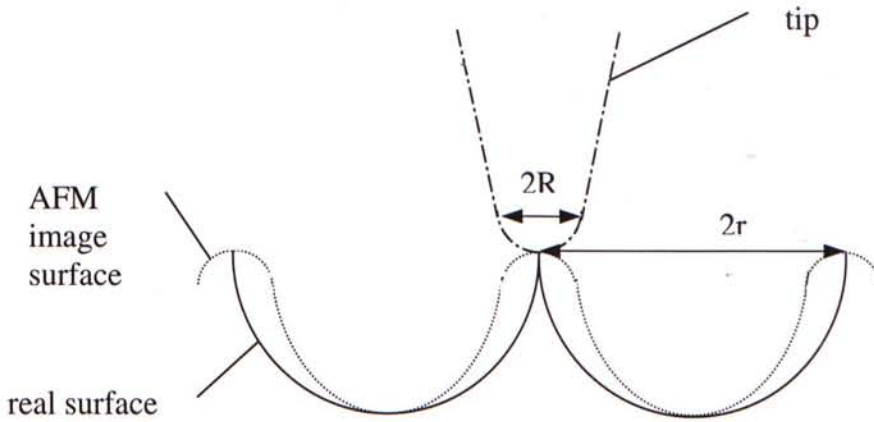

(b) R>r or R≈r

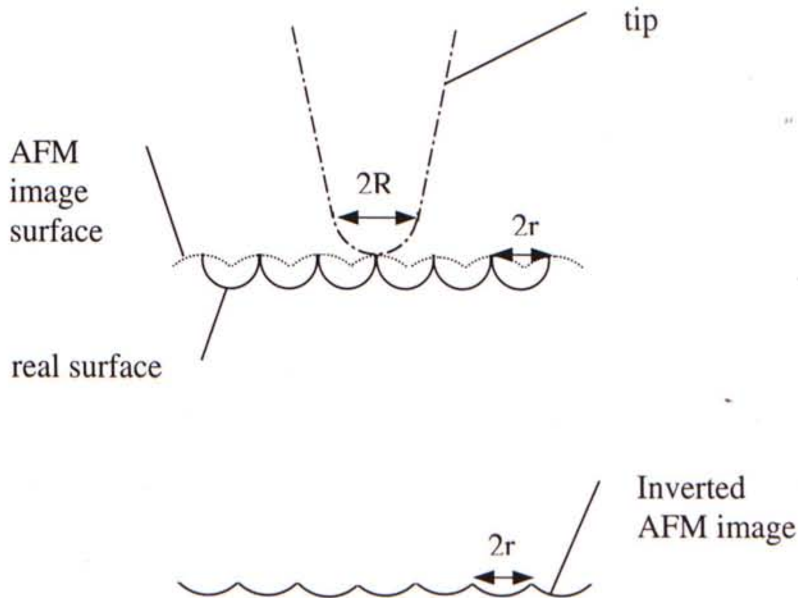

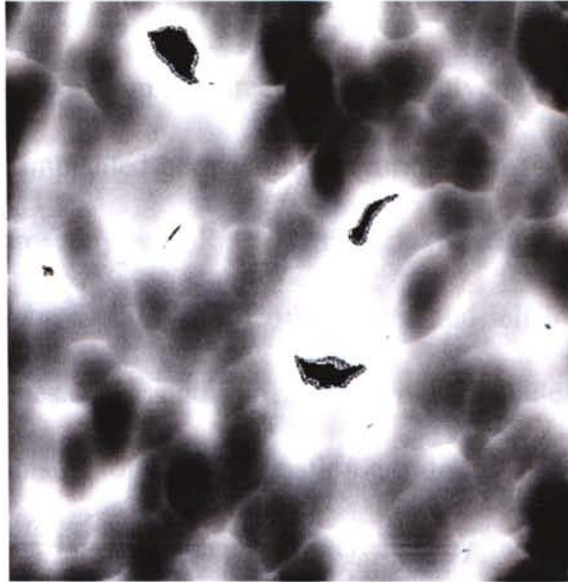

Fig. 6.4 An inverted image of Fig. 6.1 (a)

6.4. Conclusions

Contact-mode AFM was used to observe the nanostructures created on Ge surfaces by Co-ion implantation in the previous experiments. It was demonstrated that the appearance of a granular morphology obtained by contact mode is due to severe image distortions when the tip size is larger than the mean crater diameter. For images observed by tapping mode AFM, low to medium dose samples (up to 1×10^{16} ions cm^{-2}) may upon to minor image distortions. These tip artifacts can be deconvoluted by inverting the image and the lateral extension of the hole can be reproduced with reasonable accuracy.

CHAPTER 7 CONCLUSIONS

Conclusions drawn from the three projects are given below:

(1) Ion beam implanted germanium by various ion species has been studied by atomic force microscopy, and Rutherford backscattering spectrometry. Cellular nanostructures were observed on both Co-implanted and self-implanted samples, but not in C-implanted ones. This is attributed to the much smaller mass and size of C-ions. Various mechanisms for crater formation are discussed, with special attention paying to whether the larger crater can be created by the coalescence of smaller craters in medium dose implantation (10^{15} – 10^{16} ion cm^{-2}), and also the importance of the thermal spike effect in crater formation. By using Kinchin-Pease displacement damage function and Monte Carlo simulation, the mean diameter of a single cascade can be approximated to be around 11 - 25 Å, depending on the particular charge of ions. The mean crater diameter observed from AFM micrographs is an order of magnitude larger. Therefore, it is at least not contradictory to the suggested crater formation mechanism. The mean energy deposited per atom, θ_D, in a collision cascade is calculated to be around 0.05 – 0.15 eV, corresponding to a temperature around 60 - 880°C, which is still below the heat of fusion of Ge. Therefore the thermal spike effect may not be playing an active role in crater formation in our experiment. Ion channeling spectra for C-implanted samples show a smaller depth of damaged layer than the Co-implanted and self-implanted samples in higher dose implantation (6×10^{16} – 6×10^{17} ion cm^{-2}). It is suggested that because of the porous complex structure shown on the Co-implanted and self-implanted surfaces, projectiles get less chance to be bombarded, thus results in a deeper depth of damaged layer than it would be for a flat surface. A surface yield deficit exists in the

random spectra of Co-implanted, and self-implanted samples which makes it impossible to fit the spectra without introducing impurities into the near surface region.

(2) Cobalt germanides can be formed directly by high mean current density Co-ion implantation without postannealing. Because the high mean current density can readily produce the high temperatures required for the formation of various phases. MEVVA ion source implantation provides a possible manufacturing technique requiring only one single step. From XRD, Co_3Ge_2, Co_5Ge_7 and $CoGe_2$ were formed in the as-implanted samples. The first phase formed and the order of formation of various phases follow that predicted by thermodynamics, although more than one phase may form in one time. Dramatic cellular and columnar nanostructures were observed in the low and high mean current density samples respectively. RBS reveals a yield deficit in the near surface region which may be attributed to the stopping cross-section not following strictly the Bragg rule, or the decrease of Ge density due to the cellular and porous structures.

(3) Contact-mode AFM was used to observe the nanostructures created on Ge surfaces by Co-ion implantation in the previous experiments. It was demonstrated that the appearance of a granular morphology obtained by contact mode is due to severe image distortions when the tip size is larger than the mean crater diameter. For images observed by tapping mode AFM, low to medium dose samples (up to 1×10^{16} ions cm^{-2}) may upon to minor image distortions. These tip artifacts can be deconvoluted by inverting the image and the lateral extension of the hole can be reproduced with reasonable accuracy.

BIBLIOGRAPHY

1. S. M. Sze, "VLSI Technology" (McGraw-Hill, Singapore, 1983)
2. K. N. Tu and J. W. Mayer, "Thin Films Interfaces and Reaction" (Wiley, New York, 1978), 359
3. K. M. Yu, B. Katz, I. C. Wu, and I. G. Brown, "Formation of iridium silicide layer by high does iridium ion implantation into silicon", Nucl. Instr. and Meth B58 (1991), 27
4. Michael Nastasi, James W. Mayer, and James K. Hirvonen, "Ion-solid Interactions: Fundamental and Applications" (Cambridge University Press, London 1996)
5. Leonar, C. Feldman, James W. Mayer, "Fundamentals of Surface and Thin Film Analysis" (North-Holland)
6. J. Lindhard and M. Scharff, "Energy Dissipation by Ions in the keV Region", Phys. Rev., 24 (1961), 128
7. I. H. Wilson, "The Topography of Ion Bombarded Surfaces", Surface Topography, 2 (1989), 289
8. P. Sigmund, "Sputtering by Particle Bombardment I: Applied Physics" (Springer-Verlag, Berlin 1981), 9
9. Stewart, A. D. G. and Thompson, M. W., J. Mat. Sci., 4 (1969), 56
10. J. R. Parsons and C. W. Hoelke , "Radiation Effects in Semiconductors" (Plenum, New York, 1968), 339
11. J. B. Mitchell, J. A. Davies, L. M. Howe, R. S. Walker, K. B. Winterbon, G. Foti and J. A. Moore, "Ion Implantation in Semiconductors" (Plenum, New York, 1975), 493

12. R. S. Walker and D. A. Thompson, Nucl. Instr. and Meth. 135 (1976), 489

13. L. M. Howe, M. H. Rainville, H. K. Haugen and D. A. Thompson, Nucl. Instr. and Meth. 170 (1980), 419

14. L. M. Howe and M. H. Rainville, Nucl. Instr. and Meth. 182/183 (1981), 143

15. I. H. Wilson, "The effects of self-ion bombardment (30-500 keV) on the surface topography of single-crystal germanium", J. Appl. Phys. 53 (March, 1982), 1698

16. B. R. Appleton, O. W. Holland, J. Narayan, O. E. Schow. III, J. S. Williams, K. T. Short, and E. Lawson, "Characterisation of damage in ion implanted Ge", Appl. Phys. Lett. 41 (1982), 711

17. O. W. Holland, B. R. Appleton, and J. Narayan, "Ion implantation damage and annealing in germanium", J. Appl. Phys. 54 (1983), 2295

18. B. R. Appleton, O. W. Holland, D. B. Poker, J. Narayan, and D. Fathy, Nucl. Instru. Meth. B 7/8 (1985), 639

19. R. M. Feenstra and G. S. Oehrlein, "Surface Morphology of oxidized and ion-etched silicon by scanning tunneling microscopy", Appl. Phys. Lett. 47(2) (1985), 97

20. I. H. Wilson, N. J. Zheng, U. Knipping, and I. S. T. Tsong, "Effects of isolated atomic collision cascades on SiO_2/Si interfaces studied by scanning tunneling microscopy", Phys. Rev. B 38 (1988), 8444

21. I. H. Wilson, N. J. Zheng, U. Knipping, and I. S. T. Tsong, "Scanning tunneling microscopy of an ion-bombarded PbS(001) surface", Phys. Appl. Phys. Lett. 53 (1988), 2039

22. L. Porte, M. Phaner, C. H. de Villeneuve, N. Moncoffer, and J. Tousset, "Scanning tunneling microscopy study of single-ion impacts on graphite surface", Nucl. Instr. Meth. B 44 (1989), 116

23. T. Michely, K. H. Besocke, and G. Comsa, Surf. Sci. Lett. 230 (1990), L135

24. C. A. Lang, C. F. Quate, and J. Nogami, Appl. Phys. Lett. 59 (1991), 1696

25. D. C. Parks, R. Bastas, R. W. Schmieder, and M. Stockli, J. Vac. Sci. Technol. B13 (1995), 941

26. I. H. Wilson, Y. J. Chen, J. B. Xu, "Single ion impacts on an $In_{0.22}Ga_{0.78}As$/GaAs(100) surface observed by atomic force microscopy", Nucl. Instr. Meth. B (1997)

27. Y. J. Chen, I. H. Wilson, J. B. Xu, and Lin Libin, "An STM and AFM study of the effects of 1.8 MeV electron bombardment on the surface of graphite", Journal of Materials Science (1997)

28. Y. J Chen, I. H. Wilson, W. Y. Cheung, J. B. Xu, and S. P. Wong, "Ion implanted nanostructures on Ge(111) surfaces observed by atomic force microscopy", J. Vac. Sci. Technol. B15(4) (1997), 809

29. Y. J. Chen, W. Y. Cheung, I. H. Wilson, S. P. Wong and J. B. Xu, "A study of ion bombarded nanostructures on germanium surfaces by scanning tunneling microscopy", Thin Solid Film, 308/309 (1997), 415

30. André Anders, "The periodic table of vacuum arc charge state distribution", Physical Review E, 55(1) (1997), 969

31. B. R. Appleton, O. W. Holland, D. B. Poker, J. Narayan and D. Fathy, Nucl. Instrum. Methods B 7/8, (1985), 639

32. H. H. Andersen, Appl. Phys. 18 (1979), 131

33. R. S. Walker, and D. A. Thompson, Nucl. Instr. and Meth. 135 (1976), 489

34. L. Hoffmann, J. C. Bach, and B. Bech Nielsen, P. Leary and R. Jones, and S. Öberg, "Substitutional carbon in germanium", Physical Review B Vol 55 No. 17 (1997), 11 167

35. Lawrence R. Doolittle, "Algorithms for the rapid simulation of Rutherford Backscattering spectra", Nucl. Instr. and Meth. in Phy. Res. B9, (1985), 344

36. L. Van den hove, R. Wolters, K. Maex, R. F. Dekeersmaecker, and G. J. Declerck, IEEE Trans. Electron Devices, ED-34 (1987), 554.

37. M. E. Alperin, T. C. Holloway, R. A. Haken, C. D. Gosmeyer, R. V. Karnaugh, and W. D. Parmanite, IEEE Trans. Electron Devices, ED-32 (1985), 141.

38. L. Van den hove, R. Wolters, K. Maex, R. Dekeersmaecker and G. Declerck, J. Vac. Sci. Technol. B4 (1986), 1358.

39. G. L. Patton, S. S. Lyer, S. L. Delage, S. Tiwari and J. M. C. Stork, IEEE Electron Device Lett. 9 (1988), 165.

40. Y. Rajekarunanayake and J. C. McGill, Appl. Phys. Lett. 55 (1989), 1537.

41. S. P. Ashburn, M. C. Ozturk, J. J. Wortman, G. Harris, J. Honeycutt, and D. M. Maher, J. Electron. Mater. 21 (1992), 81.

42. S. P. Ashburn, M. C. Ozturk, G. Harris, and D. M. Maher, J. Appl. Phys. 74(7) (1993), 4455.

43. I. G. Brown, J. E. Gavin, and R. A. MacGrill, Appl. Phys. Lett. 47 (1985), 358.

44. The interplanar spacings are matched with those listed in JCPDS, card no. 30-435, 29-474, 4-545, 7-162.

45. W. Xia, C. A. Hewett, M. Fernandes, S. S. Lau, and D. B. Poker, J. Appl. Phys, 65(6) (1989), 2300.

46. Rui-Qing Li, Can. Metall. Q, 29(4) (1990), 279.

47. M. Hansen, K. Anderko, Constitution of Binary Alloys (McGraw Hill, New York, 1958), p. 476.

48. Q. Peng, S. P. Wong, J. B. Xu, and I. H. Wilson, Mat. Res. Soc. Symp. Proc. Vol. 396 (1996), 763.

49. Automatic fitting program for RBS spectra written by the University of Surrey Ion Beam Centre, June (1998).

50. O. W. Holland, B. R. Appleton, and J. Narayan, J. Appl. Phys. 54(5) (1983), 2295.

51. J. E. Griffith, D. A. Grigg, M. J. Vasile, P.E. Russel, and E. A. Fitzgerald, J. Vac. Sci. Technol. B9, (1991) 3596

52. G. Reiss, J. Vancea, H. Wittmann, J. Zweck, and H. Hoffmann, J. Appl. Phys. 67 (1990), 1156

53. E. J. V. Loenen, D. Dijkkamp, A. J. Hoeven, J. M. Lenssinck, and J. Dieleman, Appl. Phys. Lett. 56 (1990), 1755

54. K. L. Westra, D. J. Thomson, "Atomic force microscope tip radius needed for accurate imaging of thin film surfaces", J. Vac. Sci. Technol. B 12(6), (1994), 3176

55. F. Atamny, A. Baiker, "Direct imaging og the tip shape by AFM", Surface Science 323 (1995), L314

56. Samuel Dongmo, Michel Troyon, and Philippe Vautrot, Etienne Delain, Noel Bonnet, "Blind restoration method of scanning tunneling and atomic force microscopy images", J. Vac. Sci. Technol. B 14(2), (1996) 1552

57. Y. J. Chen, I. H.Wilson, C. S. Lee, and J. B. Xu, M. L. Yu, "Tip artifacts in atomic force microscope imaging of ion bombarded nanostructures on germanium surfaces", J. Appl. Phys. 82 (11) (1997), 5859

58. I. G. Brown, J. E. Galvin, B. F. Gavin, and R. A. MacGill, "Metal vapor vacuum arc ion source", Rev. Sci. Instrum. 57 (6) (1985), 1069

59. I. G. Brown "Vacuum Arc Ion Charge-Sate Distributions", IEEE Trans. of Plasma Sci. 19(5) (1991), 713

60. A. Wittkower, J. K. Hirvonen, "Some practical aspects of ion implantation for wear reduction", Nucl. Instr. and Meth. in Phy. Res. B6, (1985), 78

61. D. H. Zhu, B. X. Liu, "Formation of Ti silicides by metal-vapour vacuum arc ion source implantation", J. Appl. Phys. 77(12) (1995), 6257

62. Ian G. Brown, "Vacuum arc ion sources", Rev. Sci. Instrum, 65(10) (1994), 3061

63. Sun Bieha, Xiang Hongwen, "Studies on MEVVA ion source", Review of Sci. Instru. 69(2) (1998), 816

64. I. G. Brown, B. Feinberg and J. E. Galvin, "Multiply stripped ion generation in the metal vapour vacuum arc", J. Appl. Phys, 63(10) (1988), 4889

65. James E. Galvin, I. G. Brown and Robert A. MacGill, "Charge state distribution studies of the metal vapor vacuum arc ion source", Rev. Sci. Instrum, 61(1) (1990), 583

66. Ian. G. Brown, "On the current Intensity Limit of a Vacuum-Arc Ion Source", IEEE Tran. on Plasma Sci. PS-15(4) (1987), 346

67. Zhang Huixing, Zhang Xiaoji, Zhou Fengsheng, Zhang Shenji, Li Qiang, and Han Zhuen, "The Beijing metal vapor vacuum arc ion source program", Rev. Sci. Instrum. 65 (10) (1994), 3088

68. Sun Biehe, Hu Shangbin, Chen Qin, and Shui Yongqin, "Development of MEVVA ion source", Rev. Sci. Instrum. 65(4) (1994), 1266

69. I. G. Brown, "Vacuum Arc Ion CHarge-State Distribution", IEEE Tran. on Plasma Sci. 19(5) (1991), 713

70. F. S. Zhou, X. Y. Wu, F. Zhou, H. X. Zhang, and X. J. Zhang, "Measurement of some parameter on MEVVA ion source", Rev. Sci. Instrum. 85(4) (1994), 1263

71. Y. J. Chen, Doctoral Thesis for CUHK, (1997), 49

72. S. Morito, "Introduction to Scanning Probe Microscope" (Soc. Industrial Investigations, Tokyo, 1993)

73. R. Wiesendanger, :Scanning Probe Microscopy and Spectroscopy: Methods and Applications" (Cambridge Univ. Press, Cambridge, 1994)

74. C. Joachin and S. Gauthier (eds.), "Scanning Probe Microscopy: Beyond the Images" (Les Editions de Physique, 1992)

75. H. K. Wickramasinghe (ed.), "Scanning Probe Microscopy, AIP Conference Proceedings 241" (American Institute of Physics, New York, 1992)

76. Joseph R. Tesmer, Michael Nastasi (ed.), J. Charles Barbour, Carl J. Maggiore, James W. Mayer (contributing editors), "Handbook of Modern Ion Beam Materials Analysis" (Materials Research Society, Pittsburgh, 1995)

77. B. D. Cullity, "Elements of X-ray Diffraction" (Addison-Wesley Publishing Co. Inc., U.S.A., 1978)

PUBLICATIONS

Title: An investigation of implantation synthesized cobalt germanide by ion beam analysis and scanning probe microscopy

I.H. Wilson, Y. J. Chen, C. S. Lee, and W. Y. Cheung

Poster presentation at the Thirteenth International Conference on Ion Beam Analysis (IBA-13)

Title: Tip artifacts in atomic force microscope imaging of ion bombarded nanostructures on germanium surfaces

Y. J. Chen, I. H. Wilson, C. S. Lee, J. B. Xu, and M. L. Yu

Published in J. Appl. Phys 82(11) (1997), 5859

Title: Ion Beam Synthesized Cobalt Germanide Alloy By Metal Vapour Vacuum Arc Implantation

C. S. Lee, I. H. Wilson, W. Y. Cheung, Y. J. Chen, J. B. Xu and S. P. Wong

Poster presentation at the Fourteenth International Conference on Ion Beam Analysis (IBA-14)

Published in Nuclear Instruments and Methods B 148 (1999), 604-609

CUHK Libraries

003723608